



Designer molecules of the synaptic organizer MDGA1 reveal 3D conformational control of biological function

Received for publication, January 10, 2023, and in revised form, February 21, 2023. Published, Papers in Press, March 7, 2023.
<https://doi.org/10.1016/j.jbc.2023.104586>

Hubert Lee^{1,2,†}, Nicolas Chofflet^{3,4,†}, Jianfang Liu^{5,†}, Shanghua Fan^{1,2}, Zhuoyang Lu⁵, Martin Resua Rojas³, Patrick Penndorf³, Aaron O. Bailey⁶, William K. Russell⁶, Mischa Machius^{1,2}, Gang Ren^{5,*}, Hideto Takahashi^{3,4,7,8,*}, and Gabby Rudenko^{1,2,*}

From the ¹Department of Pharmacology and Toxicology, University of Texas Medical Branch, Galveston, TX, USA; ²Sealy Center for Structural Biology and Molecular Biophysics, University of Texas Medical Branch, Galveston, TX, USA; ³Synapse Development and Plasticity Research Unit, Institut de Recherches Cliniques de Montréal, Montréal, Quebec, Canada; ⁴Integrated Program in Neuroscience, McGill University, Montreal, Quebec, Canada; ⁵The Molecular Foundry, Lawrence Berkeley National Laboratory, Berkeley CA, USA; ⁶Department of Biochemistry and Molecular Biology, University of Texas Medical Branch, Galveston, TX, USA; ⁷Department of Medicine, Université de Montréal, Montréal, Quebec, Canada; ⁸Division of Experimental Medicine, McGill University, Montréal, Quebec, Canada

Reviewed by members of the JBC Editorial Board. Edited by Roger Colbran

MDGAs (MAM domain-containing glycosylphosphatidylinositol anchors) are synaptic cell surface molecules that regulate the formation of trans-synaptic bridges between neurexins (NRXNs) and neuroligins (NLGNs), which promote synaptic development. Mutations in MDGAs are implicated in various neuropsychiatric diseases. MDGAs bind NLGNs *in cis* on the postsynaptic membrane and physically block NLGNs from binding to NRXNs. In crystal structures, the six immunoglobulin (Ig) and single fibronectin III domains of MDGA1 reveal a striking compact, triangular shape, both alone and in complex with NLGNs. Whether this unusual domain arrangement is required for biological function or other arrangements occur with different functional outcomes is unknown. Here, we show that WT MDGA1 can adopt both compact and extended 3D conformations that bind NLGN2. Designer mutants targeting strategic molecular elbows in MDGA1 alter the distribution of 3D conformations while leaving the binding affinity between soluble ectodomains of MDGA1 and NLGN2 intact. In contrast, in a cellular context, these mutants result in unique combinations of functional consequences, including altered binding to NLGN2, decreased capacity to conceal NLGN2 from NRXN1 β , and/or suppressed NLGN2-mediated inhibitory presynaptic differentiation, despite the mutations being located far from the MDGA1–NLGN2 interaction site. Thus, the 3D conformation of the entire MDGA1 ectodomain appears critical for its function, and its NLGN-binding site on Ig1–Ig2 is not independent of the rest of the molecule. As a result, global 3D conformational changes to the MDGA1 ectodomain *via* strategic elbows may form a molecular mechanism to regulate MDGA1 action within the synaptic cleft.

MDGA1 and MDGA2 (MAM domain-containing glycosylphosphatidylinositol [GPI] anchor 1 and 2) are synaptic cell surface molecules found on the postsynaptic membrane (1). MDGAs are composed of six immunoglobulin (Ig) domains, a fibronectin III (FN3) domain, and a MAM (mepripin, A-5 protein, receptor protein-tyrosine phosphatase μ) domain that is tethered to the membrane by a GPI anchor (Fig. 1A). MDGAs are thought to disrupt the formation of trans-synaptic bridges between presynaptic neurexins (NRXNs) and postsynaptic neuroligins (NLGNs) that span the synaptic cleft (1). These bridges play critical roles in boosting synapse development and regulating synapse function (2–4). When MDGAs bind to NLGNs expressed together *in cis* on the postsynaptic membrane, they directly block NLGNs from recruiting NRXNs into trans-synaptic bridges and thereby from clustering the presynaptic protein machinery that is necessary for presynaptic differentiation (Fig. 1B) (5–8). A “selectivity code” has been proposed for MDGA action, whereby MDGA1 regulates NLGN2, whereas MDGA2 affects both NLGN1 and NLGN2 but ultimately impacts NLGN1 more (5–7, 9). NLGN2 is found exclusively at inhibitory synapses, whereas NLGN1 is prevalent at excitatory synapses (10–12). Insights from an extensive array of cell-based and *in vivo* studies are consistent with such a general code and suggest that MDGA1 can suppress inhibitory synapse development (by disrupting the NRXN–NLGN2 complex), whereas MDGA2 can suppress predominantly excitatory synapse development (by disrupting the NRXN–NLGN1 complex) (5–7, 9); however, in practice, it may be more complicated (13, 14). Biochemical studies have highlighted the complexities of demonstrating such an MDGA selectivity code on a molecular level (8), and little is known about the molecular mechanisms of MDGA action in general.

Genetic abnormalities of MDGAs, NLGNs, and NRXNs are implicated in the pathogenesis of neuropsychiatric disorders, such as autism spectrum disorders, schizophrenia (SZ), and bipolar disorder (1, 15–19). Furthermore, dysfunction of MDGAs, NLGNs, and NRXNs appears to alter excitation/

[†] Co-first authors.

* For correspondence: Gabby Rudenko, garudenk@utmb.edu; Hideto Takahashi, Hideto.Takahashi@ircm.qc.ca; Gang Ren, gren@lbl.gov.

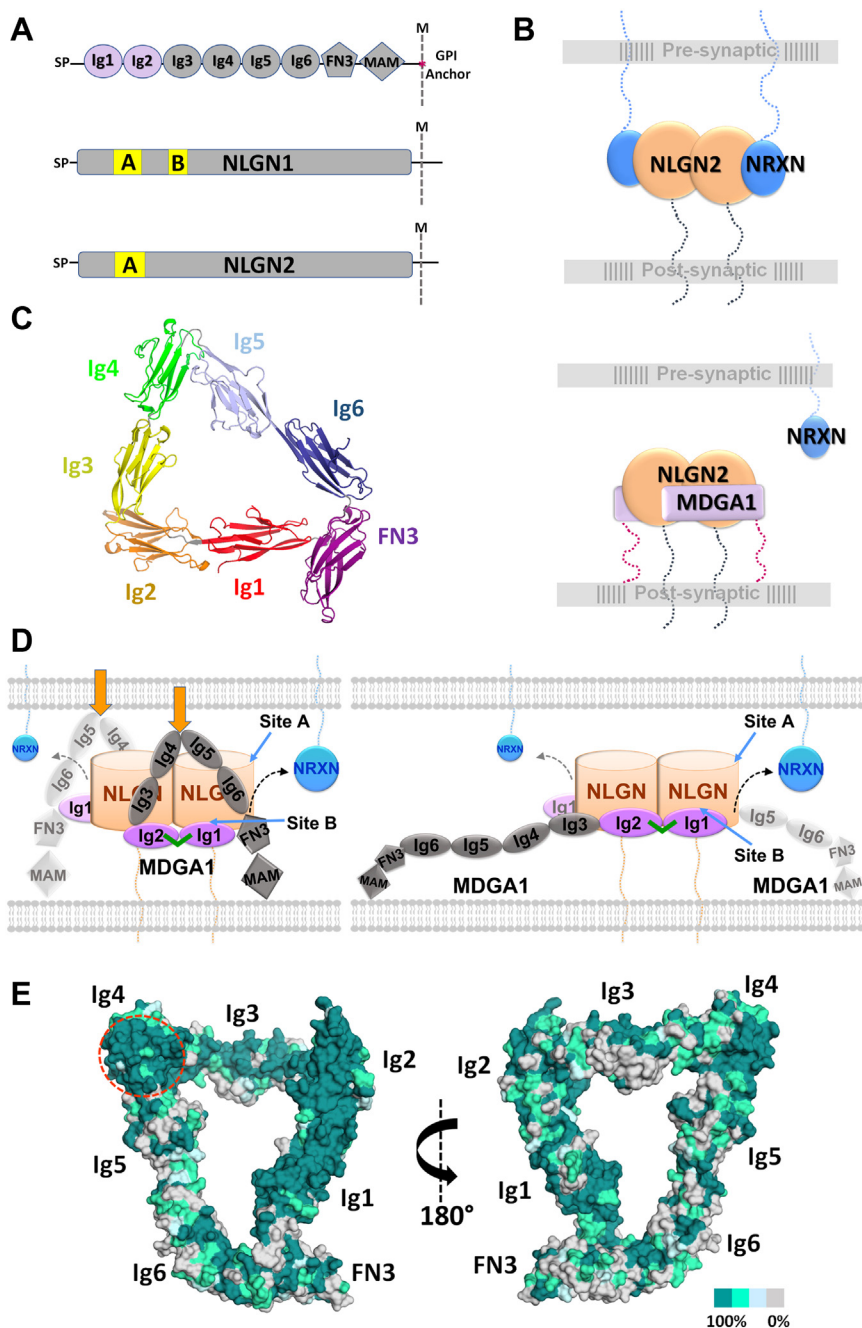


Figure 1. MDGA1 and its interaction with NLGNs. *A*, domain structure of MDGA1, NLGN1, and NLGN2. NLGN2-interacting domains in MDGA1 are highlighted in *lilac*. *B*, cartoon schematics depicting NRXN–NLGN2 trans-synaptic bridges promoting inhibitory synapses (*top*) and MDGA1 negatively regulating NRXN–NLGN2 trans-synaptic bridges by blocking the NRXN-binding site on NLGN2 (*bottom*). *C*, MDGA1 (Ig1–FN3) adopts a triangular shape in the crystal structure (Protein Data Bank ID: 5OJ2). *D*, possible conformations of MDGA1 interacting with NLGNs tethered in the synaptic cleft as explored in this study. Compact MDGA1 conformation (*left*); elongated conformation (*right*). *Orange arrows* (*left panel*) point to a region with high sequence conservation of surface residues in Ig4 near the Ig4–Ig5 elbow as shown in *E*. The naturally occurring interdomain disulfide bond between MDGA1 Ig1 and Ig2 is shown in *green*. The NLGN2-interacting domains Ig1 and Ig2 are highlighted in *purple* in MDGA1. NLGN splice inserts site A and site B are discussed in the text. *E*, sequence conservation of 212 vertebrate MDGA1 sequences mapped onto the MDGA1 crystal structure (Protein Data Bank ID: 5OJ2). Surface colors indicate decreasing levels of surface sequence conservation ranging from *teal* (100% identity), *green*, and *light cyan* to *gray* (nonconserved). A region of high sequence conservation on Ig4 is highlighted with a *dashed red oval*. M, membrane; SP, signal peptide. FN3, fibronectin III; Ig1, immunoglobulin 1; MDGA, MAM domain–containing glycosylphosphatidylinositol anchor; NLGN, neuroligin; NRXN, neurexin.

inhibition balances in brain circuits, disrupting—for instance—neural circuits critical for cognition and behavior (1, 3, 4, 7, 9, 20). These proteins are uniquely positioned to dynamically modulate the excitation/inhibition ratio because of their selective localization to excitatory *versus* inhibitory synapses and

their roles in regulating synapse development and function (2, 21–23). Thus, it is of paramount importance to delineate the mechanism of MDGAs, their interactions with NLGNs, and their impact on synapse development to understand their roles in neural circuits and in related disease states.

Some atomic details of the mode of interaction between MDGAs and NLGNs are now known from X-ray crystallographic studies (8, 24, 25). They reveal that the MDGA1 Ig1–Ig2 tandem contains a binding site for NLGNs that straddles the NLGN dimer with MDGA1 Ig1 binding to one NLGN monomer and MDGA1 Ig2 binding to the other; a second MDGA1 molecule engages the NLGN dimer on the opposite side with symmetrical interactions. The NLGN dimer is thus sandwiched between two MDGA1 molecules with all four membrane-bound tethers (two each from MDGA1 and NLGN) emanating from the same side of the protein complex. A rare interdomain disulfide bond, typically not seen between Ig domains, connects the MDGA1 Ig1–Ig2 tandem into a rigid rod-like structure (24). The surface on NLGNs where MDGA1 Ig1 binds overlaps with the site where NRXNs bind, indicating that MDGAs interfere with the formation of NRXN–NLGN trans-synaptic bridges by sterically blocking NRXNs from binding to NLGNs (24, 25). Strikingly, the MDGA1 ectodomain (minus the MAM domain) adopts a triangular shape with the three sides made up of the domain tandems Ig1–Ig2, Ig3–Ig4, and Ig5–Ig6, respectively (Fig. 1C) (8). Numerous contacts across the sharply angled Ig2–Ig3 and Ig4–Ig5 elbows appear to stabilize this conformation (8). Such a compact or “closed” triangular shape is also observed in an X-ray crystal structure of MDGA1 in complex with NLGN1 (8).

The unusual triangular shape and uncommon interdomain disulfide bond between Ig1 and Ig2 set MDGAs apart from other synaptic organizers for which high-resolution structural information is available and raise questions as to how MDGAs leverage their unique 3D structure to carry out their function. Do MDGA molecules adopt alternative conformations beyond the compact form seen in crystal structures? Does the global 3D conformation impact the ability of MDGAs to bind partners and/or the ability of MDGAs to impact synaptic function? For instance, in the compact form, the NLGN binding site on Ig1–Ig2 would be spatially constrained with respect to the rest of the molecule as well as the presynaptic membrane, a feature that would not only impact the fit of the molecule in the synaptic cleft but also potential interactions with other synaptic components. On the other hand, if MDGAs could transition to more elongated open forms, the interaction site for NLGNs would become largely independent of the rest of the molecule, and binding sites for other possible partners could become more accessible (Fig. 1D). Indeed, the surface of MDGA1 Ig4 near the Ig4–Ig5 elbow is highly conserved, though far away from the highly conserved NLGN binding site on Ig1–Ig2, suggesting that it may house a binding site for an as yet unidentified partner (Fig. 1E). In the compact state, this conserved surface region faces inward toward the center of the MDGA–NLGN complex restricting its accessibility (Fig. 1D). The shape of MDGA molecules could also work as a sensor for splice inserts present at strategic structural positions in select NLGNs and contribute to the selectivity code in this manner. NLGN1 and NLGN2 can accommodate 20 to 40 residue splice inserts at “site A”; NLGN1 harbors an additional “site B” that can accommodate a nine-residue splice insert GNRWSNSTK (Fig. 1A) (2, 26–29). Site A is located far from the

NLGN–MDGA binding interface but could sterically clash with Ig6 in the triangular form of MDGA1 but less so with elongated forms (Fig. 1D). Site B in NLGN1 is located close to the NLGN–MDGA binding interface (loop $\beta 6$ – $\beta 7$), and its presence is known to decrease MDGA–NLGN interaction likely because of steric clashes (8, 24) (Fig. 1D). Thus, the domain arrangement in MDGA1 molecules is poised to have fundamental impacts on the biological function of MDGA1.

Here, we investigated structure–function relationships for MDGAs using both full-length, membrane-bound, as well as a soluble non–membrane-bound MDGA1. We first probed the soluble ectodomain of MDGA1 WT using a series of biophysical and structural techniques and established that it can adopt both compact (“closed”) and more elongated (“open”) forms. We then engineered a panel of mutant MDGA1 molecules aimed at promoting elongated or compact forms, respectively, by targeting the Ig2–Ig3 and Ig4–Ig5 elbows. We probed the ability of purified, soluble, non–membrane-bound ectodomains of MDGA1 WT and mutants to bind NLGN2 in solution as well as that of full-length and membrane-bound MDGA1 WT and mutants to recruit NLGN2 and to shield NLGN2 from NRXN binding and to induce synapse formation in cell-based assays. Collectively, our results establish that (1) MDGA molecules can adopt both compact and elongated conformations with specific elbows working together to produce the overall shape of the molecule; (2) the shape of MDGAs can be regulated *via* strategic designer mutants targeting specific molecular elbows; and (3) our MDGA1 mutants uniquely impact the ability to bind and shield NLGN2 at the cell surface and to block NLGN2-induced GABAergic presynaptic differentiation (compared with MDGA1 WT), despite their more or less normal physical interactions with NLGN2. Together, our data show that the global 3D conformation of MDGA1 fundamentally impacts its function and that the individual domains work in synergy.

Results

MDGA1 WT adopts compact and elongated forms

To probe the conformational variability of MDGA1 WT, we first purified its soluble ectodomain following baculovirus-mediated overexpression in High Five insect cells (Fig. S1). We then probed the conformational diversity of MDGA1 molecules by size-exclusion chromatography (SEC) under both high salt (HS, buffer containing 500 mM NaCl) and low salt (LS, buffer containing 50 mM NaCl) conditions. Under HS conditions, MDGA1 WT eluted as a broad peak with a major species at 1.47 ml elution volume (EV), corresponding to a Stokes radius (R_s) of ~ 5.4 nm and an apparent molecular weight ($M_{w,app}$) of ~ 190 kDa assuming a globular shape (Figs. 2A and S2A). The calculated M_w ($M_{w,calc}$) of MDGA1 is ~ 104 kDa based on the amino acid sequence; our purified MDGA1 has an M_w of ~ 112 kDa by mass spectrometry (MS) with the difference accounting for post-translational modifications. Under LS conditions, MDGA1 eluted as a broad peak with a major species at EV = 1.53 ml, corresponding to an R_s of ~ 4.3 nm and an $M_{w,app}$ of ~ 119 kDa (Figs. 2A and S2A).

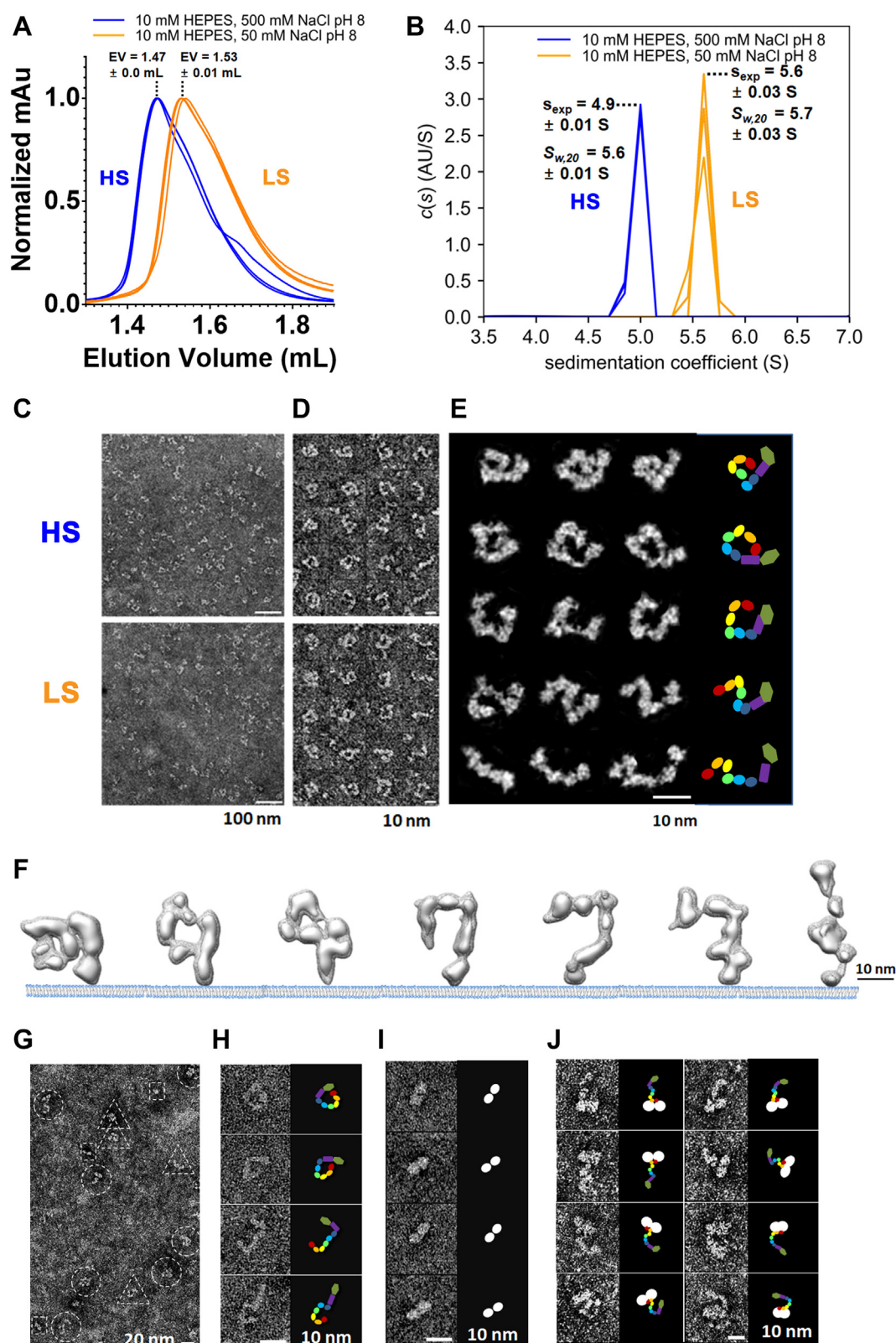


Figure 2. MDGA1 adopts compact and elongated conformations. *A*, size-exclusion chromatography (SEC) elution profiles of MDGA1 WT at low ionic strength (LS, 50 mM NaCl; orange lines) and high ionic strength (HS, 500 mM NaCl; blue lines). Samples are shown in triplicate; peak heights are set to 1.0 to normalize the data for the protein amount loaded. Calibration standards run in triplicate deviated <0.02 ml between runs (Fig. S2A). *B*, sedimentation coefficient distribution for MDGA1 WT from SV-AUC under LS (orange lines) and HS (blue lines) conditions. Samples are shown in triplicate. The average sedimentation coefficient s_{exp} as well as standardized values, $S_{w,20}$ are indicated. *C*, negative-staining electron microscopy (NS-EM) of MDGA1 WT under HS (top) and LS (bottom) conditions in survey micrographs. *D*, 20 representative particles boxed from micrographs under HS (top) and LS (bottom) conditions. *E*, zoom-ins of 15 selected particles from the HS sample (after particle-shaped masking) with accompanying cartoon schematics reveal an ensemble of conformations. *F*, 3D reconstruction of seven individual MDGA1 WT particles (HS sample) by individual-particle electron tomography (IPET) displayed with

The asymmetric and broadened peak for MDGA1 (compared with structurally homogenous particles, such as calibration markers) under both HS and LS conditions suggests that the protein migrates as an ensemble of conformations. The differences in the peak location between the HS and LS conditions may also reflect differences in molecular shape, though differential interactions of the protein with the gel matrix at low ionic strength can also influence the migration behavior. By sedimentation velocity analytical ultracentrifugation (AUC), an orthogonal method characterizing particles free in solution, MDGA1 WT sedimented as a single species with a sedimentation coefficient s_{exp} of 4.9 ± 0.01 S under HS conditions and an s_{exp} of 5.6 ± 0.03 S under LS conditions, which when converted to standardized sedimentation coefficients corresponded to more similar values of $S_{20,w}$ of 5.6 ± 0.01 S (HS) and $S_{20,w}$ of 5.7 ± 0.03 S (LS), respectively (Figs. 2B and S2B). These data are compatible with MDGA1 molecules occupying a range of different conformations.

To visualize the conformation of individual MDGA1 WT molecules directly, we used negative-staining EM (NS-EM) of the soluble ectodomains (Fig. 2, C–F). High-contrast images suitable for the analysis and quantification of particles were obtained using HS buffer conditions (Fig. 2C, top panel, Table S1). Particles were selected and grouped into sufficiently similar conformations permitting the calculation of reference-free class averages (Fig. S2C). Roughly 60% of the MDGA1 WT molecules adopted a compact form under HS conditions, whereas the rest adopted a range of elongated forms. Images could also be obtained under LS conditions, but the particles appeared blurrier, making class averages less reliable so that quantitative comparison between HS and LS conditions was not warranted (Fig. 2C, bottom panel, Table S1 and Fig. S2C). Qualitatively, however, the data allowed the conclusion that MDGA1 particles can adopt a wide range of distinctive shapes (under both HS and LS conditions), including elongated and V-shapes, as well as triangular-shaped molecules similar to those seen in crystal structures (Protein Data Bank [PDB] ID: 5OJ2 and 5OJ6) (Fig. 2, D and E). The variation of MDGA1 molecular shapes was also studied using individual particle electron tomography (IPET) (30), which enabled us to calculate 3D reconstructions of single molecules. 3D density maps from seven representative individual particles under HS conditions showcased the wide range of different MDGA1 WT molecular shapes (Figs. 2F and S3). Taken together, MDGA1 forms an ensemble of molecules containing “compact” as well as more “elongated” shapes.

We then assessed by NS-EM whether both compact and more elongated forms of MDGA1 WT could bind to NLGN2(+A) (NLGN2 containing splice insert A) (Fig. 2, G–J

and Table S1). Of 1828 particles analyzed from 23 micrographs, 40% (730 particles) consisted of the MDGA1–NLGN2(+A) complex, whereas 31% (567 particles) contained MDGA1 and 29% (531 particles) contained NLGN2(+A). The majority of the complexes contained MDGA1 in a non-compact form (80%; 581 particles). Interestingly, the unliganded MDGA1 molecules were predominantly in the compact form (62%, 352 particles). Thus, soluble MDGA1 WT and NLGN2(+A) ectodomains appear bound to each other regardless of whether the MDGA1 molecules are compact (as seen in the crystal structure) or more elongated (as seen by NS-EM).

Engineering MDGA1 molecules with altered 3D conformation

To probe whether the overall conformation of the MDGA1 ectodomain affects its biological function, we designed mutations that would favor either compact or more elongated MDGA1 conformations while leaving the direct binding site for NLGN2 intact. Based on the interdomain interactions observed in the triangular-shaped MDGA1 crystal structure (PDB ID: 5OJ2), the Ig1–Ig2, Ig3–Ig4, and Ig5–Ig6 tandems appear comparatively rigid, whereas the regions between them resemble molecular hinges. We thus focused on the Ig2–Ig3 and Ig4–Ig5 elbows for our mutants as observed in the crystal structure (Fig. 3A). The MDGA1 Ig2–Ig3 elbow is near the NLGN2 binding site on the MDGA1 Ig1–Ig2 tandem, and it remains kinked also in the crystal structure of the MDGA1 Ig1–Ig2–Ig3 fragment (25). The MDGA1 Ig4–Ig5 elbow is near the surface of Ig4 that exhibits high sequence conservation (Fig. 1E). To promote closed elbows, we engineered single disulfide bonds connecting adjacent Ig domains in a way that would constrain the relative domain orientations. To promote elongated forms, we engineered mutations that introduce a negatively charged residue in the hydrophobic core that is present at each elbow.

To select suitable residues for mutagenesis, we examined the interactions between the domains at each elbow (Fig. 3B). The Ig2–Ig3 elbow is formed by the Ig2 and Ig3 domains packing against each other *via* two key β -strands/loops tethered by the linker residues T²³⁰–T²³⁶. Key residues for this packing are T¹³⁵, V¹³⁶, and H¹³⁷ in Ig2 and N³¹³, V³¹⁴, and G³¹⁵ in Ig3 (Fig. 3C). In addition, a prominent hydrophobic core is formed by F²³¹ surrounded by L¹³⁴, V¹³⁶, V¹⁵³, L¹⁵⁵, and L²³³ in Ig2 and T²³⁷, P²⁶⁹, and V³¹⁴ in Ig3 (Fig. 3C). Replacement of T¹³⁵ and N³¹³ each with cysteines was compatible with the formation of a disulfide bond clamping Ig2 and Ig3 together, which would stabilize the Ig2–Ig3 interface (Fig. 3C). By contrast, the mutation MDGA1 V³¹⁴D would bury a negative charge in the hydrophobic core of the interface likely

respect to a membrane. G–J, NS-EM of MDGA1–NLGN2(+A) complexes in 10 mM Hepes (pH 8.0), 50 mM NaCl, 3 mM CaCl₂. G, survey micrographs of representative MDGA1 (triangle), NLGN2 (square), and MDGA1–NLGN2 complex particles (circle). H–J, zoom-ins of particles with corresponding cartoon representations: H, four representative particles of MDGA1 in different conformations. I, four representative NLGN2 particles. J, eight representative MDGA1–NLGN2 complexes. Scale bars are indicated in C–J. In E, F, H, and J, the N- and C-terminal ends of the molecule are putatively assigned based on the fact that the C-terminal MAM domain forms a larger globular domain than the N-terminal Ig1 domain. In the cartoons in (E, H and I), and (J), the MDGA1 domains are represented by rainbow colors from Ig1 (red oval) through the MAM domain (forest green hexagonal), and the NLGN2 dimer is shown as a white dumbbell shape. HS, high salt; Ig, immunoglobulin; LS, low salt; MAM, meprin, A-5 protein, receptor protein-tyrosine phosphatase μ ; MDGA, MAM domain-containing glycosylphosphatidylinositol anchor; NLGN, neuroligin; SV-AUC, sedimentation velocity analytical ultracentrifugation.

disrupting the hydrophobic key interaction between F²³¹ (Ig2) and V³¹⁴ (Ig3) promoting the Ig2–Ig3 elbow to open (Fig. 3C). The Ig4–Ig5 elbow, which involves S⁴³⁴–T⁴³⁷ tethering the Ig4 and Ig5 domains, features key residues from Ig4 (β-strand T³³³–I³³⁶) and Ig5 (loop N⁵¹⁹–N⁵²²) (Fig. 3D). F⁵²¹ in Ig5 is buried in a hydrophobic pocket formed by I³³⁶, P³³⁸, and T³⁴⁷ at the Ig4–Ig5 interface (Fig. 3D). Also, a salt bridge between E³⁴⁵ in Ig4 and R⁵²⁶ in Ig5 spans the interface (Fig. 3D). Replacement of T³³³ and Y⁵¹⁹ each with cysteines was compatible with the formation of a disulfide bond clamping Ig4 and Ig5 together, which would stabilize the Ig4–Ig5 interface (Fig. 3D). On the other hand, MDGA1 I³³⁶D would bury a negative charge in the hydrophobic core of the Ig4–Ig5 interface promoting an open Ig4–Ig5 elbow (Fig. 3D). Thus, it was possible to generate mutants that target specific elbows in MDGA1 that

would be predicted to promote “compact” or more “elongated” states, respectively.

Molecular conformation of MDGA1 mutants

The hexahistidine-tagged soluble ectodomains of our four designer MDGA1 molecules (T¹³⁵C/N³¹³C, V³¹⁴D, T³³³C/Y⁵¹⁹C, and I³³⁶D) were overexpressed in insect cells using a baculovirus-mediated system and purified (Fig. S1). The mutant proteins under HS conditions were subjected to SEC to characterize their size distributions (Fig. 4, A–D) and imaged using NS-EM to visualize individual molecules as well as calculate reference-free class averages to evaluate the ensembles of conformations (Figs. 4, E–H, S4 and Table S1). The two mutants incorporating a disulfide bond, MDGA1 T¹³⁵C/

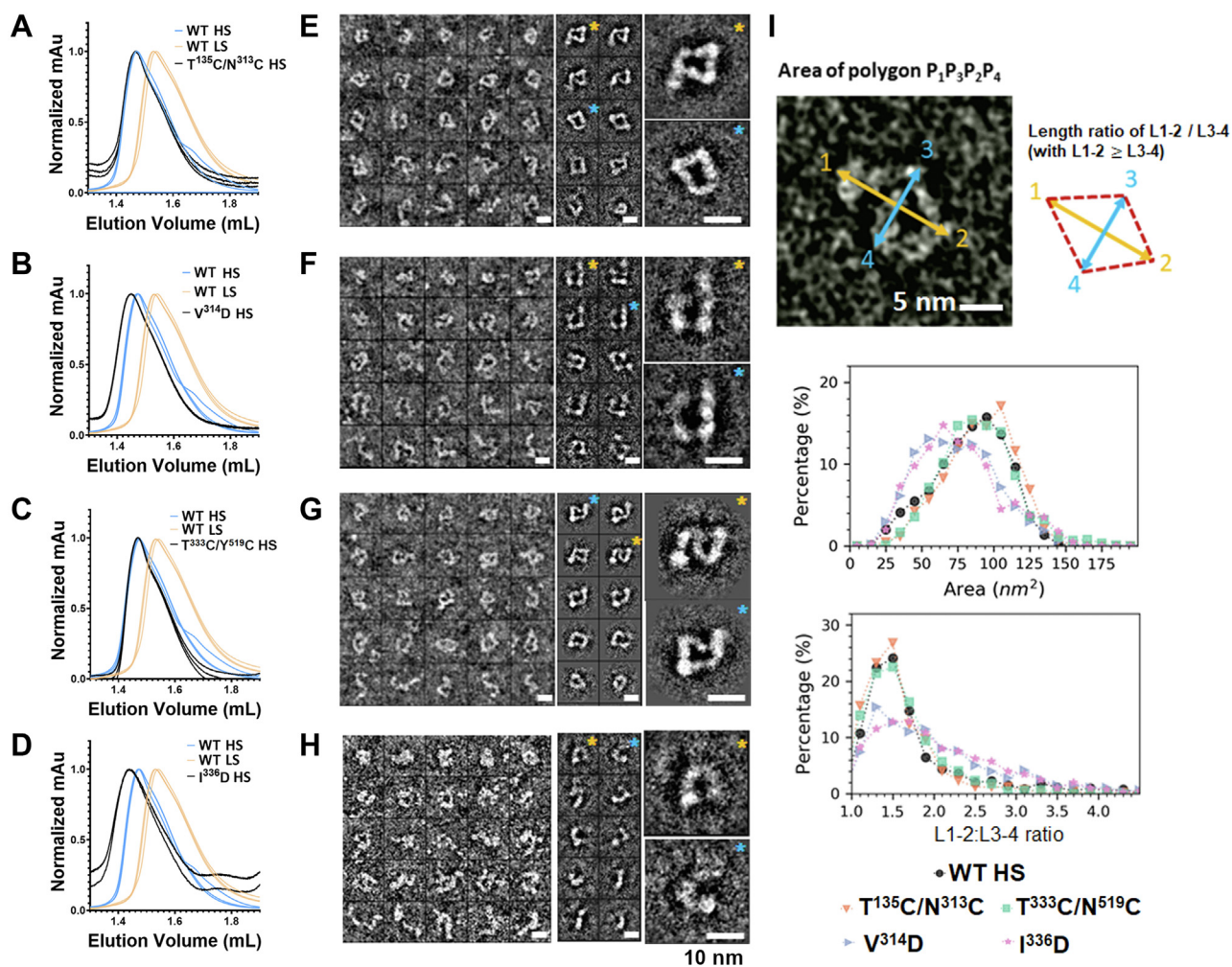


Figure 4. Analysis of MDGA1 mutants by SEC and NS-EM. A, MDGA1 T¹³⁵C/N³¹³C SEC elution profile. B, MDGA1 V³¹⁴D SEC elution profile. C, MDGA1 T³³³C/Y⁵¹⁹C SEC elution profile. D, MDGA1 I³³⁶D SEC elution profile. For the SEC studies in A–D, the samples were run in triplicate. MDGA1 mutants at high ionic strength (HS) are shown as black curves. MDGA1 WT at high ionic strength (WT HS) in blue curves and MDGA1 WT at low ionic strength (WT LS) in orange curves are taken from Figure 2. E, MDGA1 T¹³⁵C/N³¹³C examined by NS-EM under high ionic strength conditions (HS; 500 mM NaCl). Shown are 25 representative particles (left panel), 10 selected reference-free class averages (middle panel), and two zoomed-in class averages with the best contrast (right panel). F, MDGA1 V³¹⁴D shown as described in B. G, MDGA1 T³³³C/Y⁵¹⁹C shown as described in C. H, MDGA1 I³³⁶D shown as described in D. Scale bars are indicated in E–H and represent 10 nm; the pairs of a reference-free class average and its zoom-in are indicated with color-coded asterisks. I, conformational distribution of a quadrilateral polygon (1234) in two perpendicular directions whereby dimension L1–2 is longer than dimension L3–4. Histograms of the particle size distribution (area of polygon 1234, red colored dashed line) and particle shape distribution (ratio L1–2:L3–4) are shown. The numbers of particles used for each analysis are MDGA WT (800); MDGA1 T¹³⁵C/N³¹³C (421); MDGA1 V³¹⁴D (473); MDGA1 T³³³C/Y⁵¹⁹C (896); and MDGA1 I³³⁶D (399). HS, high salt; LS, low salt; MDGA, MAM domain-containing glycosylphosphatidylinositol anchor; NS-EM, negative-staining EM; SEC, size-exclusion chromatography.

$N^{313}C$ (Ig2–Ig3) and MDGA1 $T^{333}C/Y^{519}C$ (Ig4–Ig5), produced ensembles of molecules that were very similar to MDGA1 WT with SEC peak positions (EV of 1.47 ml) and similar peak broadening (Fig. 4, A and C). By NS-EM, MDGA1 $T^{135}C/N^{313}C$ and $T^{333}C/Y^{519}C$ adopted a range of different molecular shapes, but like MDGA1 WT, compact forms were the most prevalent (Fig. 4, E, G and I). MDGA1 $T^{333}C/Y^{519}C$ (Ig4–Ig5) was further analyzed by tryptic peptide mapping followed by MS revealing that the engineered MDGA1 $T^{333}C/Y^{519}C$ disulfide bond indeed formed to $\sim 85\%$. Suitable tryptic peptides to assess MDGA1 $T^{135}C/N^{313}C$, however, could not be generated (Fig. S5). The two mutants incorporating a charged residue designed to open molecular elbows, MDGA1 $V^{314}D$ (Ig2–Ig3) and MDGA1 $I^{336}D$ (Ig4–Ig5), produced ensembles of molecules that appeared more elongated compared with MDGA1 WT: by SEC, the major peaks for MDGA1 $V^{314}D$ (EV of 1.45 ml) and MDGA1 $I^{336}D$ (EV of 1.44 ml) were shifted to smaller EVs compared with WT (Fig. 4, B and D), and in NS-EM, more molecules with extended conformations were observed compared with WT (Fig. 4, F, H and I). Taken together, while MDGA1 $T^{135}C/N^{313}C$ and MDGA1 $T^{333}C/Y^{519}C$ did not significantly alter the average distribution of MDGA1 shapes or prevent the transition to more elongated shapes that HS conditions trigger, MDGA1 $V^{314}D$ and MDGA1 $I^{336}D$ were each sufficient to measurably alter the distribution of molecular shapes and promote elongated shapes, as concluded from both the SEC and NS-EM studies. Thus, the molecular shape of MDGA1 can be engineered, and strategic mutations at the Ig2–Ig3 and Ig4–Ig5 elbows can be leveraged to alter the distribution of MDGA1 conformations.

MDGA1 mutations impact the cell-surface binding of partners

To determine the impact of our designer MDGA1 mutations on biological function, we used a panel of cell-based assays to assess the interaction of MDGA1 (WT or mutants) with NLGN2. In cell-surface binding assays, we monitored the ability of soluble NLGN2 ectodomain proteins fused to human immunoglobulin Fc region (NLGN2-Fc) with or without the site A insert (GPLTKKRDEATLNPPDT; NLGN2(+A) and NLGN2(-A), respectively) to bind to the surface of COS7 cells expressing extracellularly hemagglutinin-tagged, membrane-bound MDGA1 WT or mutants (Fig. 5A; approach 1). MDGA1 WT and the mutants expressed at comparable levels on the cell membrane (Fig. 5B). CD4, an unrelated cell-surface protein that does not bind NLGNs, was used as the negative control (6, 7) (Fig. 5B). All four MDGA1 mutants showed striking differences in their ability to bind to soluble NLGN2(+A) and NLGN2(-A) compared with MDGA1 WT (Fig. 5, C–F). At the Ig2–Ig3 elbow, $T^{135}C/N^{313}C$ and $V^{314}D$ both largely abolished the ability of membrane-bound MDGA1 to bind soluble NLGN2(+A) ($\sim 4\%$ of WT, decreasing by $95.6 \pm 0.5\%$ SEM for $T^{135}C/N^{313}C$ and $\sim 10\%$ of WT, decreasing by $89.6 \pm 1.7\%$ SEM for $V^{314}D$, respectively) (Fig. 5, C and D). At the Ig4–Ig5 elbow, $T^{333}C/Y^{519}C$ also significantly decreased the ability to bind NLGN2(+A) ($\sim 40\%$ of WT, decreasing by $61.2 \pm 3.2\%$ SEM) (Fig. 5, C and D). By

contrast, $I^{336}D$ had strongly increased NLGN2(+A) binding ($\sim 190\%$ of WT, increasing by $88.9 \pm 13.8\%$ SEM) (Fig. 5, C and D). Identical trends were observed for the MDGA1 mutants binding to splice-insert-free NLGN2(-A), indicating that the mutants were not sensitive to the site A insert (Fig. 5, E and F). Taken together, covalently stabilizing the Ig tandems at the Ig2–Ig3 or the Ig4–Ig5 elbow decreased the ability of membrane-bound MDGA1 to bind soluble NLGN2. By contrast, the effect of opening up the tethered MDGA1 molecule depended on which elbow is manipulated; opening the Ig2–Ig3 elbow strongly decreased the ability to bind soluble NLGN2, whereas opening the Ig4–Ig5 elbow strongly increased binding.

To further validate the impact of the mutations on NLGN2 binding, we reversed the soluble and tethered partners in our assay and monitored the binding of soluble hexahistidine-tagged MDGA1 WT and mutants to NLGN2(+A) expressed on the surface of COS7 cells (Fig. 5A; approach 2). Strikingly, when presented as a soluble ectodomain, only the mutations opening up the elbows had large effects on the ability of MDGA1 to bind to NLGN2 (Fig. 5, G and H). Soluble MDGA1 $V^{314}D$ remained unable to efficiently bind tethered NLGN2(+A) ($\sim 10\%$ of WT, decreasing by $89.8 \pm 1.5\%$ SEM) (Fig. 5, G and H). By contrast, soluble MDGA1 $I^{336}D$ again bound tethered NLGN2(+A) much better ($\sim 500\%$ of WT, increasing by $408.4 \pm 14.6\%$ SEM) (Fig. 5, G and H). Soluble MDGA1 $T^{135}C/N^{313}C$ (Ig2–g3 elbow)-bound surface-tethered-NLGN2(+A) as well as MDGA1 WT, whereas MDGA1 $T^{333}C/Y^{519}C$ (Ig4–Ig5 elbow) bound less well ($\sim 75\%$ of WT, decreasing by $23.9 \pm 3.8\%$ SEM).

Taken together, our designer mutants impact the ability of MDGA1 to bind to NLGN2 in distinctive ways despite the mutated residues residing outside the NLGN2-binding site on the Ig1–Ig2 tandem. Some mutants decrease and others increase NLGN2 binding in cell-surface binding assays (e.g., MDGA1 $V^{314}D$ versus MDGA1 $I^{336}D$). Some mutants depend on their context as tethered or as soluble ectodomains, whereas others do not (e.g., the impact of MDGA1 $T^{135}C/N^{313}C$ is tethering sensitive, whereas that of MDGA1 $V^{314}D$ is not). Finally, mutants with a similar structural impact can exert opposite effects on NLGN2 binding depending on their exact location in the molecule (e.g., MDGA1 $V^{314}D$ versus MDGA1 $I^{336}D$). Taken together, these results suggest that not only the overall global shape of MDGA1 but also its orientation and/or presentation on the cell plasma membrane impact its ability to bind to NLGN2.

MDGA1 mutations impact biological function

We next tested whether our designer mutants could bind NLGN2(+A) *in cis* on the cell surface and block NRXN1 binding in cell-based competition assays (Fig. 6A). MDGA1 mutants that bind NLGN2 worse than WT would be expected to leave more NLGN2 molecules unmasked on the cell surface enabling more soluble NRXN1 to be recruited. Likewise, MDGA1 mutants binding NLGN2 better than WT would be expected to block NRXN1 more than MDGA1 WT or at least as well. We coexpressed extracellularly hemagglutinin-tagged

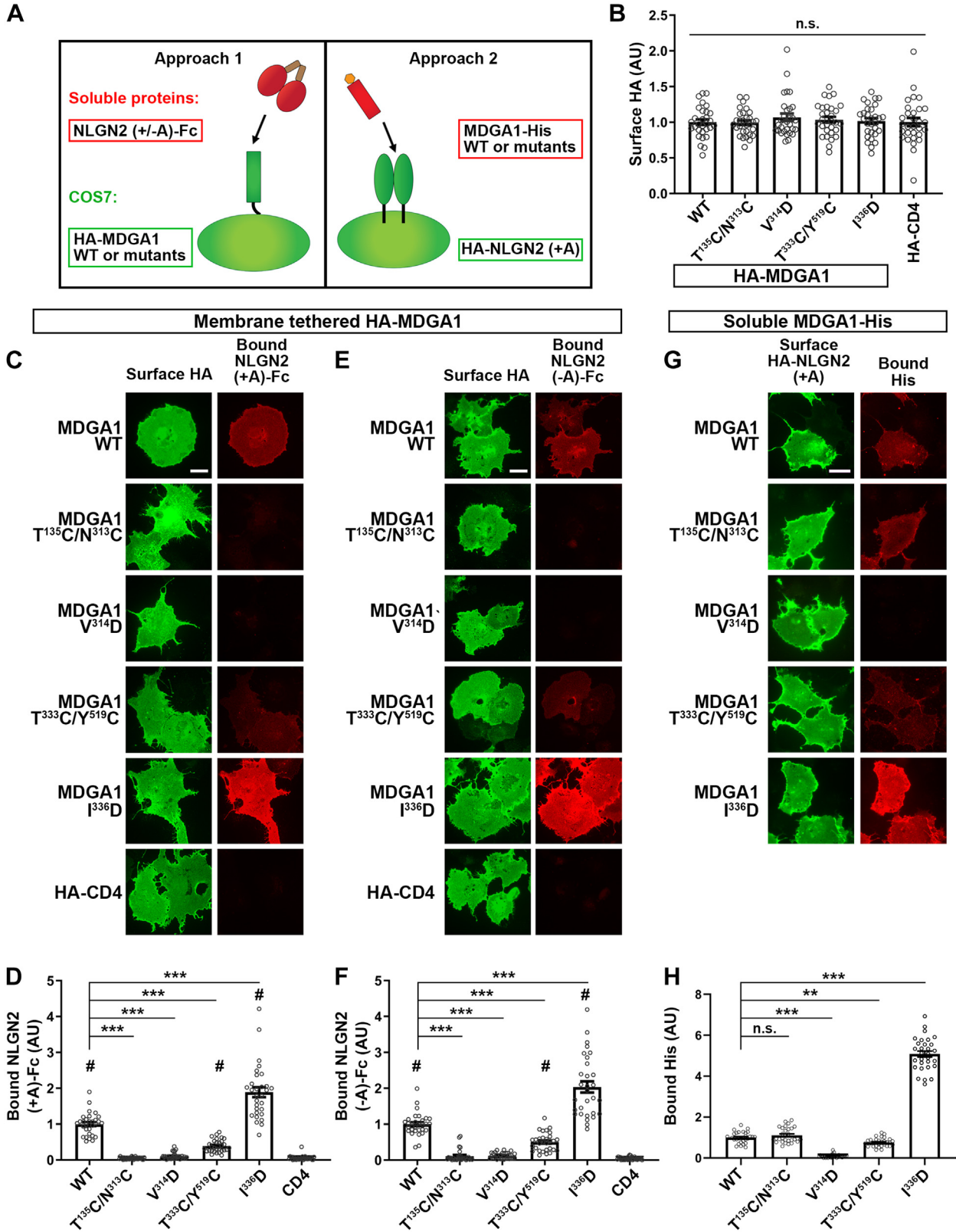


Figure 5. MDGA1 mutants display altered interaction with NLGN2 in cell surface-binding assays. *A*, cell-based assays used to test the interaction of MDGA1 WT or mutants with NLGN2(±A). In approach 1 (*left panel*), hemagglutinin (HA)-tagged membrane-bound MDGA1 WT or mutants are expressed on the surface of COS7 cells, and soluble NLGN2(±A) Fc-fusion proteins (50 nM) are added to the cell cultures. In approach 2 (*right panel*), HA-tagged NLGN2(+A) is expressed on the surface of COS7 cells, and soluble (His)6-tagged MDGA1 WT or mutants (200 nM) are added to the cell cultures. *B*, quantification of the expression of HA-MDGA1 WT, HA-MDGA1 mutants, and HA-CD4 on the surface of COS7 cells normalized to the value for HA-MDGA1 WT. Three independent experiments were carried out for each condition (N = 10 cells per experiment; Welch's ANOVA; *p* value = 0.567). *C*, representative fluorescence images of soluble NLGN2(+A)-Fc bound to HA-MDGA1 WT or mutants expressed on COS7 cells or HA-CD4 as a negative control. *D*, quantification of NLGN2(+A)-Fc bound to transfected cells described in *C*. The bound NLGN2(+A)-Fc signal is divided by the HA surface signal and normalized to

MDGA1 (HA-MDGA1) WT or mutants with extracellularly Myc-tagged NLGN2(+A) (myc-NLGN2(+A)) *in cis* on the surface of COS7 cells and assessed the amount of soluble NRXN1 β that is recruited (expressed as an Fc-fusion protein and lacking the splice insert SS4; NRXN1 β (-SS4)-Fc) (Fig. 6, B and C). In parallel, the transmembrane molecule CD4 was also coexpressed with Myc-NLGN2(+A) as control and used to normalize the data by giving the maximal amount of NRXN1 β that could bind in the absence of MDGA1-mediated suppression (*i.e.*, 0% blocked, 100% NRXN1 β binding). MDGA1 WT and mutants expressed similarly on the cell surface (3.9% differences) as did NLGN2 coexpressed with each MDGA1 form (4.4% differences, except NLGN2 in combination with MDGA1 V³¹⁴D that was decreased by 16.8 \pm 5.7% SEM (*p* value of 0.006, Fig. 6, D and E). In line with the cell surface-binding studies described in Figure 5, coexpression of MDGA1 WT and NLGN2 on the cell surface greatly reduced the amount of NRXN1 β (-SS4)-Fc that could be recruited to ~30% of the CD4 level (representing the maximal level), decreasing by 72.8 \pm 3.9% SEM (Fig. 6, B and C).

The MDGA1 T¹³⁵C/N³¹³C and V³¹⁴D mutations engineered at the Ig2–Ig3 elbow were unable to block NLGN2 efficiently from recruiting NRXN1 β (-SS4)-Fc (decreased only to ~80% of the CD4 level, a 19.9 \pm 4.5% SEM decrease for MDGA1 T¹³⁵C/N³¹³C with *p* = 0.02 and decreased even less, to ~95% of the CD4 level, for MDGA1 V³¹⁴D, a statistically nonsignificant difference of 6.0 \pm 3.0% SEM with *p* = 0.95, Fig. 6, B and C). These competition studies are consistent with the inability of MDGA1 T¹³⁵C/N³¹³C and V³¹⁴D tethered to the cell surface to recruit NLGN2 (Fig. 5, C–F). By contrast, MDGA1 T³³³C/Y⁵¹⁹C and I³³⁶D engineered at the Ig4–Ig5 elbow blocked NLGN2 from recruiting NRXN1 β (-SS4)-Fc quite well (reducing the amount of NRXN1 β (-SS4)-Fc bound to ~55% of the CD4 level for MDGA1 T³³³C/Y⁵¹⁹C, a 44.4 \pm 4.5% SEM reduction with *p* < 0.001, and to ~40% of the CD4 level for MDGA1 I³³⁶D, a 57.5 \pm 3.5% SEM reduction with *p* < 0.001) (Fig. 6, B and C). The reduced ability of MDGA1 T³³³C/Y⁵¹⁹C to block NLGN2 is consistent with its reduced ability to bind NLGN2 when tethered to the cell surface (Fig. 5C). Although MDGA1 I³³⁶D bound more NLGN2 in cell surface-binding assays (Fig. 5C) and significantly blocked NRXN1 β binding compared with CD4, a negative control (Fig. 6, B and C), this variant was less active in blocking NRXN1 β binding than MDGA1 WT (Fig. 6, B and C), suggesting that an increase in MDGA1–NLGN2 binding may not

simply contribute to enhanced power to compete with NRXN1 β . Taken together, the competition studies suggest that manipulating the Ig2–Ig3 and Ig4–Ig5 elbows in MDGA1 not only impacts NLGN2 binding but also the ability to block NLGN2 from binding to NRXN1 β .

To assess whether the MDGA1 mutants impact inhibitory presynaptic differentiation, we performed artificial synapse formation assays using neuron-fibroblast coculture methods (Fig. 6F). HA-MDGA1 WT (or mutants) were coexpressed with Myc-NLGN2(+A) on the surface of human embryonic kidney 293T (HEK293T) cells *in cis*, and their ability to prevent NLGN2-induced GABAergic presynaptic differentiation on the axonal surface of hippocampal GABAergic interneurons was assessed (Fig. 6, G and H). The level of vesicular GABA transporter (VGAT), which loads the neurotransmitters GABA and glycine from the neuronal cytoplasm into synaptic vesicles, was used as a marker for GABAergic presynaptic differentiation. As before, noninteracting CD4 coexpressed *in cis* with NLGN2 was used as a control, in this case, to represent the maximal level of inhibitory synapse formation possible because of NLGN2 overexpression in the presence of any residual endogenous MDGAs expressed on HEK293T cells (100% induction of presynaptic differentiation). The different combinations of MDGA1 WT or mutants with NLGN2 expressed similarly on HEK293T cells (within 8% and 7%, respectively) (Fig. 6, I and J). Expression of MDGA1 WT *in cis* with NLGN2 revealed inhibitory presynaptic differentiation at ~35% of the CD4 level and decreasing VGAT levels by 64.7 \pm 5.5% SEM (Fig. 6H).

The MDGA1 mutants T¹³⁵C/N³¹³C and V³¹⁴D in the Ig2–Ig3 elbow permitted robust NLGN2-induced inhibitory presynaptic differentiation (100.9 \pm 13.0% SEM for T¹³⁵C/N³¹³C and 101.6 \pm 14.1% SEM for V³¹⁴D of CD4 levels with *p* > 0.05); thus, these mutants were completely defective in suppressing inhibitory presynaptic differentiation. MDGA1 T³³³C/Y⁵¹⁹C in the Ig4–Ig5 elbow also permitted robust inhibitory presynaptic differentiation at ~85% of the CD4 level, that is, decreased by only 13.1 \pm 12.4% SEM with *p* > 0.05, a statistically insignificant difference, indicating a defective MDGA1 molecule as well (Fig. 6H). By contrast, MDGA1 I³³⁶D decreased inhibitory presynaptic differentiation to ~45% of the CD4 level (a reduction of 53.2 \pm 9.9% SEM with *p* = 0.02) (Fig. 6H). Thus, three of our MDGA1 mutants (T¹³⁵C/N³¹³C, V³¹⁴D, and T³³³C/Y⁵¹⁹C) displayed clearly reduced abilities to block

the value for the amount bound by HA-MDGA1 WT. Three independent experiments were carried out for each condition (N = 10 cells per experiment; Welch's ANOVA with Dunnett's T3 test; *p* value of WT versus CD4 < 0.001; *p* value of T³³³C/Y⁵¹⁹C versus CD4 < 0.001; *p* value of I³³⁶D versus CD4 < 0.001; *p* value of WT versus T¹³⁵C/N³¹³C < 0.001; *p* value of WT versus V³¹⁴D < 0.001; *p* value of WT versus T³³³C/Y⁵¹⁹C < 0.001; *p* value of WT versus I³³⁶D < 0.001). E, representative images of soluble NLGN2(-A)-Fc bound to the surface of transfected COS7 cells as carried out in C). F, quantification of NLGN2(-A)-Fc bound to transfected COS7 cells described in E. Three independent experiments were carried out for each condition (N = 10 cells per experiment; Welch's ANOVA with Dunnett's T3 test; *p* value of WT versus CD4 < 0.001; *p* value of T³³³C/Y⁵¹⁹C versus CD4 < 0.001; *p* value of I³³⁶D versus CD4 < 0.001; *p* value of WT versus T¹³⁵C/N³¹³C < 0.001; *p* value of WT versus V314D < 0.001; *p* value of WT versus T333C/Y519C < 0.001; *p* value of WT versus I336D < 0.001). G, representative fluorescence images of cell surface binding of soluble MDGA1-(His)6 WT or mutants to HA-NLGN2(+A) on COS7 cells. H, quantification of MDGA1-(His)6 WT or mutants bound to transfected cells described in G. The bound (His)6 signal is divided by the HA-NLGN2(+A) surface signal and normalized to the value for the amount bound by MDGA1-(His)6 WT. Two independent experiments were used for each condition (N = 15 cells per experiment; Welch's ANOVA with Dunnett's T3 test; *p* value of WT versus T¹³⁵C/N³¹³C = 0.8707; *p* value of WT versus V³¹⁴D < 0.001; *p* value of WT versus T³³³C/Y⁵¹⁹C = 0.003; *p* value of WT versus I³³⁶D < 0.001). All data are shown as means \pm SEMs. (# *p* < 0.001 compared with CD4; n.s. *p* > 0.05; **p* < 0.05; ***p* < 0.01; ****p* < 0.001 compared with MDGA1 WT). Scale bars represent 20 μ m. MDGA, MAM domain-containing glycosylphosphatidylinositol anchor; NLGN, neuroligin; n.s., not significant.

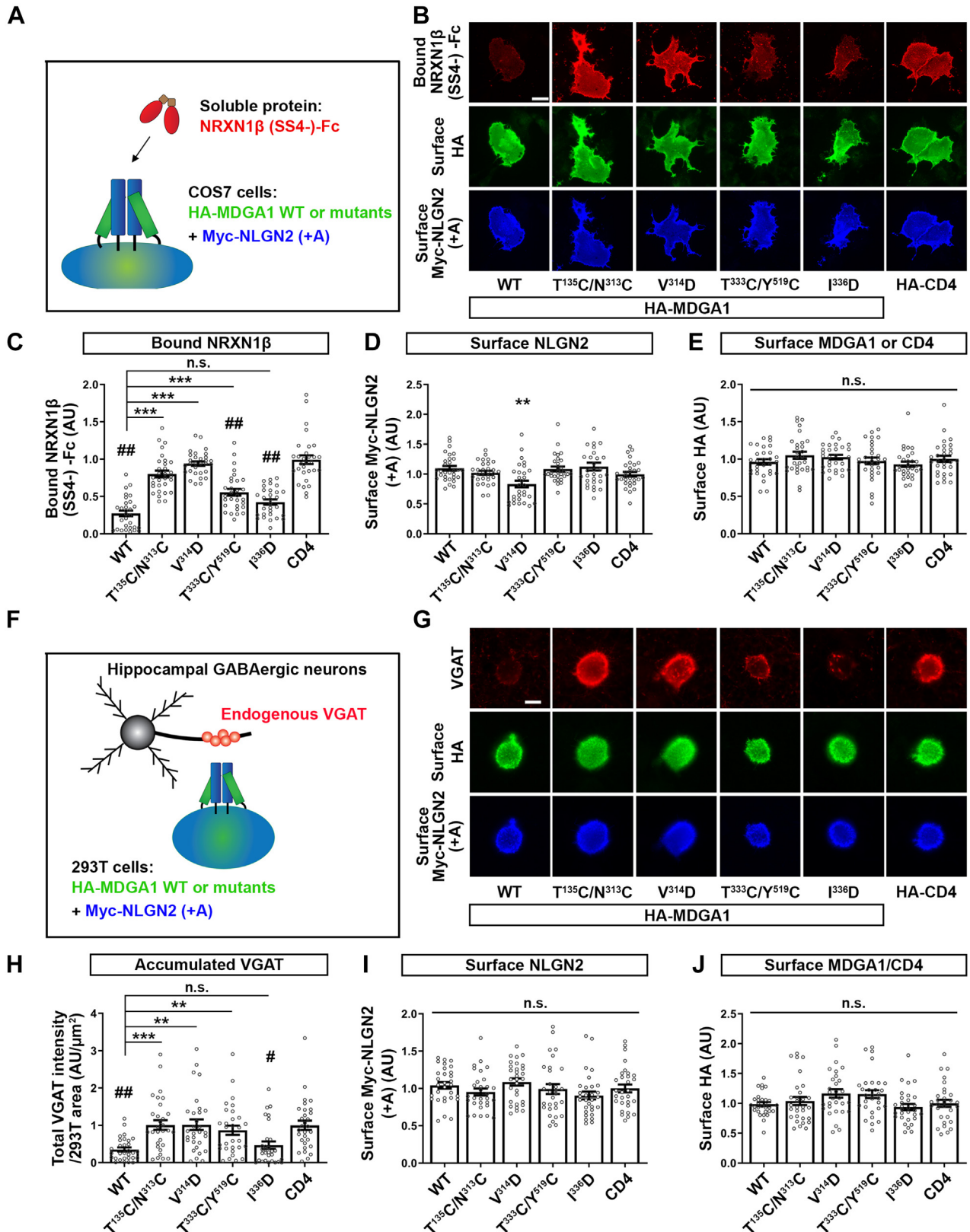


Figure 6. MDGA1 mutants display altered ability to shield NLGN2 from NRXN1 β binding and to suppress NLGN2-mediated GABAergic presynaptic differentiation. *A*, cell surface protein binding assay used to test the ability of MDGA1 to shield NLGN2(+A) from binding NRXN1 β . HA-tagged MDGA1 WT or mutants and Myc-tagged NLGN2(+A) are coexpressed in COS7 cells. Soluble Fc-tagged NRXN1 β (SS4) (100 nM) recruitment by NLGN2(+A) is assessed in a competitive cell surface-binding assay. *B*, representative fluorescence images of soluble NRXN1 β (SS4)-Fc bound to the surface of COS7 cells expressing *in cis* myc-NLGN2(+A) and HA-MDGA1 WT or mutants. As control for “no shielding,” HA-CD4 is coexpressed with myc-NLGN2(+A). The scale bar represents 20 μ m. *C*, quantification of NRXN1 β (SS4)-Fc bound to transfected cells described in *B*. The bound NRXN1 β (SS4)-Fc signal is divided by the myc-NLGN2(+A) signal and normalized to the value for the HA-CD4 coexpressing group. Three independent experiments were carried out for each condition (N = 10 cells per experiment; Welch’s ANOVA with Dunnett’s T3 test; *p* value of WT versus CD4 <0.001; *p* value of T333C/Y519C versus CD4 <0.001; *p* value of I³³⁶D versus

NRXN1 β (-SS4)-Fc binding and to suppress NLGN2-mediated GABAergic presynaptic differentiation, whereas one mutant MDGA1 I³³⁶D appeared similarly efficient as MDGA1 WT. Overall, altering the conformation of the MDGA1 ectodomain at either the Ig2–Ig3 or Ig4–Ig5 elbow can disrupt its biological function in the competition assays and artificial synapse formation assays.

MDGA1 mutations leave the direct NLGN2(+A) binding site intact

Our designer MDGA1 mutants could act through different mechanisms, for example, altering the physical interactions with NLGN2 directly, altering access to the NLGN2 binding site, or through other more complex mechanisms. To gain insight into different possible mechanisms, we tested the binding of purified immobilized MDGA1 WT (MDGA1 WT_{imm}) and our mutants to soluble NLGN2(+A) ectodomains using surface plasmon resonance (SPR) (Fig. 7). As a control for nonspecific binding, we used NLGN2(+A) Mut1, a triple mutant (H²⁷⁸A/D³⁶²K/E³⁷²K) with decreased affinity for MDGA1 because of a compromised MDGA1-binding site (24) (Figs. 7 and S6). The resulting data were fitted to a model describing a 1:1 (bimolecular) association reaction between one bound MDGA1 monomer and an NLGN dimer. Soluble NLGN2(+A) binds to MDGA1 WT_{imm} with a K_D of 3.4 ± 0.7 nM, whereas binding by NLGN2(+A) Mut1 was negligible (Figs. 7 and S6). Interestingly, the mutants located at the Ig2–Ig3 elbow (MDGA1 T¹³⁵C/N³¹³C_{imm} and V³¹⁴D_{imm}) showed somewhat worse NLGN2(+A) binding compared with MDGA1 WT. On the other hand, the mutants at the Ig4–Ig5 elbow (MDGA1 T³³³C/Y⁵¹⁹C_{imm} and I³³⁶D_{imm}) behaved very similarly to MDGA1 WT. Therefore, immobilized MDGA1 WT and the four mutants all interact with the soluble NLGN2(+A) ectodomain with relatively high affinity. The pronounced differences in NLGN2 binding affinity that we see for the MDGA1 mutants in the cell-based assays thus likely reflect the consequences of altering the global 3D molecular shape of the MDGA1 ectodomain, rather than directly altering the MDGA1–NLGN2 interaction site.

Discussion

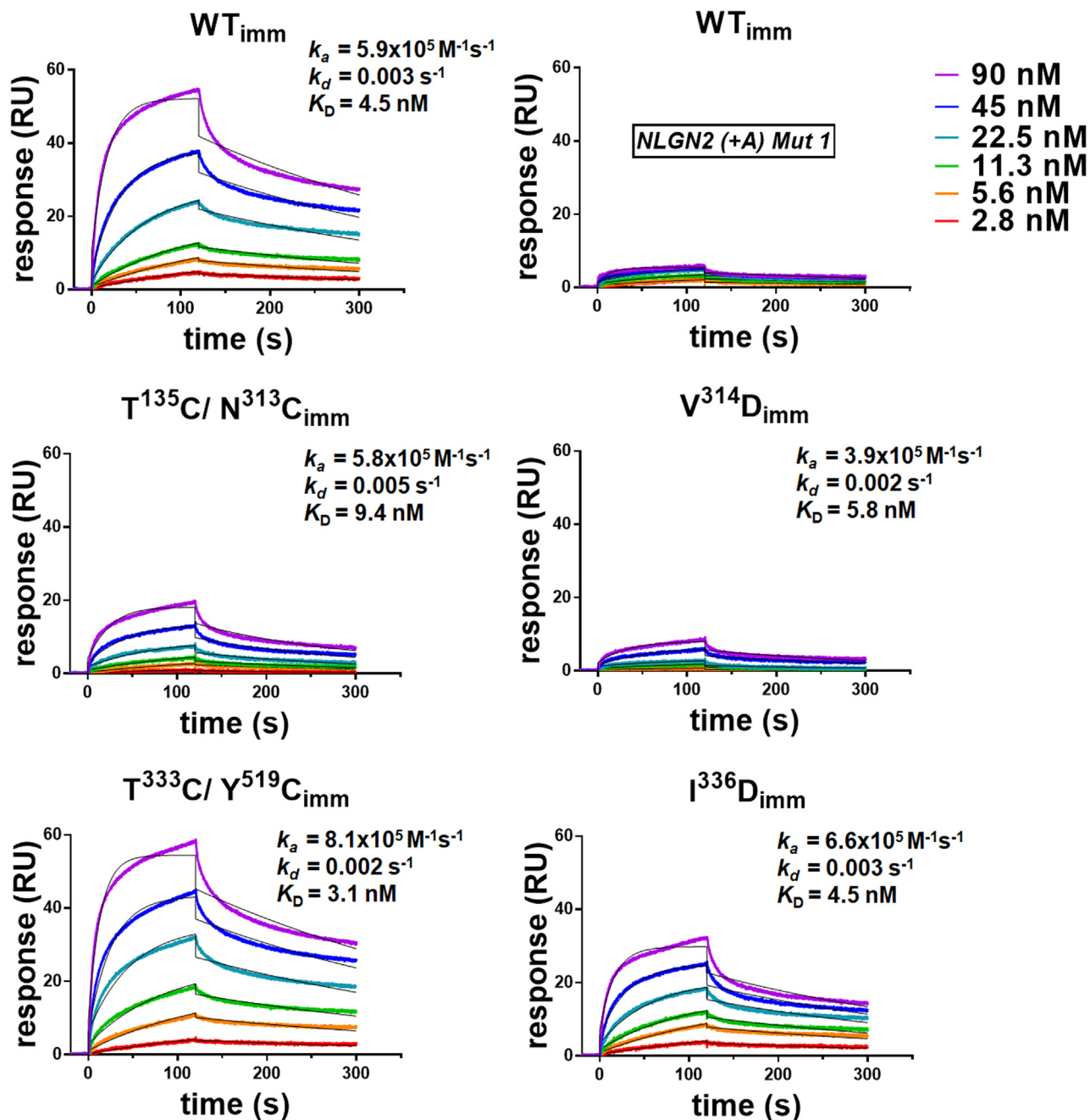
MDGA1 is a conformationally changeable molecule

Our studies reveal fundamental insights into the structure–function relationships governing MDGA1 action. While the multidomain composition of MDGAs is compatible with a “beads-on-a-string” arrangement that would render the NLGN2-binding site on MDGA1 Ig1–Ig2 freely exposed and independent of the rest of the molecule, in the crystal structures of the near complete MDGA1 ectodomain, MDGA1 Ig1–Ig2 is integrally embedded in a triangularly shaped molecule (8). We show here that as soluble (non–membrane-bound) ectodomains, MDGA1 WT can adopt both compact and elongated states and that both forms can bind NLGN2 (Fig. 2). The distribution of MDGA1 molecular shapes can be altered by varying the ionic strength, with low ionic strength conditions promoting more compact MDGA1 molecules (Fig. 2). A compact conformation is seen in the MDGA1 ectodomain crystal structure as well, which was determined at low ionic strength (<150 mM NaCl) (8). Designer mutants targeting the 3D shape of MDGA1 in a controlled way successfully alter the distribution of molecular shapes (Figs. 3 and 4). However, neither the mutations considered here nor varying ionic strength is sufficient to generate molecules that are exclusively compact or exclusively elongated. When attached to the cell surface in cell-based assays, our mutants display marked differences in action, suggesting that the 3D conformation of MDGA1 and the context in which it is presented on the plasma membrane (and by extension, the synaptic cleft) are critically important for its function (Figs. 5, 6 and 7; discussed later).

MDGA1 mutants as molecular probes for structure–function relationships

Our designer mutants work as valuable probes to delineate structure–function relationships because they target the MDGA1 molecule in unique ways and elicit characteristic effects on function (summarized in Fig. 8). Despite being located outside the binding site for NLGN2, each mutation alters the ability of MDGA1 to (1) bind NLGN2 (regardless of site A

CD4 <0.001; p value of WT versus T¹³⁵C/N³¹³C <0.001; p value of WT versus V³¹⁴D <0.001; p value of WT versus T³³³C/Y⁵¹⁹C <0.001; p value of WT versus I³³⁶D = 0.071). *D*, quantification of Myc–NLGN2(+A) expression on the surface of COS7 cells from (B) normalized to the value for the HA–CD4 coexpressing group. Three independent experiments for each condition were carried out (N = 10 cells per experiment; Welch's ANOVA with Dunnett's T3 test; p value of WT versus V³¹⁴D = 0.006). *E*, quantification of the expression of HA–MDGA1 WT, HA–MDGA1 mutants, or HA–CD4 on the surface of COS7 cells from (B) normalized to the value for the HA–CD4 coexpressing group. Three independent experiments for each condition were carried out (N = 10 cells per experiment; one-way ANOVA; p value = 0.288). *F*, artificial synapse formation assay used to test the ability of MDGA1 WT or mutants to suppress NLGN2(+A)-mediated GABAergic presynaptic differentiation. In an artificial-synapse formation assay, HEK293T cells coexpressing Myc–NLGN2(+A) and HA-tagged MDGA1 WT or mutants are cocultured with hippocampal neurons at 21 DIV for 24 h. Accumulation of the presynaptic GABAergic marker VGAT around the transfected HEK293T cells is monitored by immunofluorescence. *G*, representative images of VGAT accumulation induced by myc–NLGN2(+A) and HA–MDGA1 WT or mutants coexpressed in HEK293T cells. As control for “no suppression,” HA–CD4 is coexpressed with myc–NLGN2(+A) in the absence of MDGA1. The scale bar represents 25 μ m. *H*, quantification of the total integrated intensity of VGAT accumulated on the cell surface of HEK293T cells expressing myc–NLGN2(+A) together with the indicated HA-tagged MDGA1 protein or HA–CD4, divided by the cell surface area for each HEK293T cell and normalized to the value for the HA–CD4 coexpressing group. Three independent experiments for each condition were carried out (N = 10 cells per experiment; Welch's ANOVA with Dunnett's T3 test; p value of WT versus CD4 <0.001; p value of I³³⁶D versus CD4 = 0.021; p value of WT versus T¹³⁵C/N³¹³C <0.001; p value of WT versus V³¹⁴D = 0.001; p value of WT versus T³³³C/Y⁵¹⁹C = 0.007; p value of WT versus I³³⁶D = 0.994). *I*, quantification of Myc–NLGN2(+A) expression on the surface of HEK293T cells from (H) normalized to the value for HA–CD4 coexpressing group. Three independent experiments for each condition were carried out (N = 10 cells per experiment; one-way ANOVA; p value = 0.190). *J*, quantification of the expression of HA–MDGA1 WT, HA–MDGA1 mutants, or HA–CD4 on the surface of HEK293T cells from (H) normalized to the value for HA–CD4 coexpressing group. Three independent experiments for each condition were carried out (N = 10 cells per experiment; Welch's ANOVA; p value = 0.046). All data are shown as means \pm SEMs. (# p <0.05; ## p <0.001 compared with CD4; n.s. p > 0.05; * p < 0.05; ** p < 0.01; *** p < 0.001 compared with MDGA1 WT). HA, hemagglutinin; HEK293T, human embryonic kidney 293T cell line; MDGA, MAM domain–containing glycosylphosphatidylinositol anchor; NLGN, neuroligin; NRXN, neuroligin; n.s., not significant; VGAT, vesicular GABA transporter.



Immobilized Ligand	Analyte	$K_D \pm SD$ (nM)	Response (RU)	Immobilized (RU)	N
MDGA1 WT	NLGN2 (+A)	3.4 ± 0.7	[20 – 75]	[403 – 408]	5
MDGA1 WT	NLGN2 (+A) Mut1	n.d.	[0 – 8]	[403 – 408]	5
MDGA1 T ¹³⁵ C/N ³¹³ C	NLGN2 (+A)	13.3 ± 8.7	[7 – 23]	[413 – 425]	3
MDGA1 V ³¹⁴ D	NLGN2 (+A)	8.8 ± 4.1	[9 – 10]	[462 – 610]	4
MDGA1 T ³³³ C/Y ⁵¹⁹ C	NLGN2 (+A)	3.1 ± 0.81	[48 – 70]	[359 – 485]	4
MDGA1 I ³³⁶ D	NLGN2 (+A)	3.4 ± 1.3	[33 – 50]	[483 – 508]	4

Figure 7. MDGA1 constructs interact with NLGN2(+A) by SPR. Binding of soluble NLGN2(+A) and NLGN2(+A) Mut1 to MDGA1-coupled sensors by SPR, using a concentration range of 0 to 90 nM (top right). NLGN2(+A) Mut1 was used as the negative control to represent “no binding.” Representative sensorgrams of MDGA1 proteins (colored curves) fitted to a 1:1 bimolecular interaction model (black curves) are shown with K_D (affinity), k_a (on-rate), and k_d (off-rate) indicated. Small differences in K_D values in the table compared with those calculated from the k_a and k_d values are due to rounding effects. A table summarizes all the samples run. K_D values (Ave K_D) are averages over two independent experiments (mean \pm SD) containing a combined three to five replicates (N). “Response” (in RU) refers to the amount of the different soluble NLGN2 forms bound (Analyte). “Immobilized” (in RU) refers to the amount of the different MDGA1 forms immobilized on the C1 sensor chip (Ligand). The NLGN2 concentrations are expressed as a function of the Mw of the NLGN2 dimer because the different MDGA1s are sparsely distributed across the SPR chip and bind soluble NLGN dimers with a 1:1 stoichiometry. MDGA, MAM domain-containing glycosylphosphatidylinositol anchor; Mw, Molecular weight; NLGN, neuroligin; SPR, surface plasmon resonance.

	Shape by NS-EM	Surface binding (tethered MDGA1s)	Surface binding (soluble MDGA1s)	Competition studies	Induction synaptic differentiation	SPR Immobilized MDGA1s	Interpretation
MDGA1 WT	more compact	= (100%)	= (100%)	shields by ~73% ± 4%	blocks by ~65% ± 6%	$K_D \sim 7.1 \pm 1.4$ nM	
$T^{135}C/N^{313}C$ (Ig2-Ig3)	more compact	---	≈	--	--	≈	• membrane-tethering MDGA1 shapes NLGN2 binding
$V^{314}D$ (Ig2-Ig3)	more elongated	---	---	--	--	≈	• the orientation of Ig1-Ig2 within MDGA1 regulates NLGN2 binding
$T^{333}C/Y^{519}C$ (Ig4-Ig5)	more compact	---	≈	-	--	=	• membrane-tethering MDGA1 shapes NLGN2 binding
$I^{336}D$ (Ig4-Ig5)	more elongated	+++	+++	≈	≈	=	• the orientation of Ig1-Ig2 within MDGA1 regulates NLGN2 binding

= (same as WT); ≈ (statistically insignificant differences to WT); +++ (more than WT); -, --, --- (less than WT)

Figure 8. MDGA1 structure–function relationships. Summary of the impact of the MDGA1 mutations in our orthogonal panel of assays. MDGA, MAM domain-containing glycosylphosphatidylinositol anchor.

insert), (2) shield NLGN2 from binding to NRXN1β, and/or (3) suppress NLGN2-mediated inhibitory presynaptic differentiation in cell-based assays, in distinct ways. Furthermore, our MDGA1 mutants appear properly folded given that their cell surface expression is comparable to that of MDGA1 WT (Fig. 5B), that they show similar expression levels when coexpressed with NLGN2 (Fig. 6, E and J), and that they display similar binding affinities to NLGN2 when presented as purified soluble ectodomains in SPR studies (Fig. 7). Our studies reveal binding affinities between MDGA1 WT and NLGN2(+A) by SPR ($K_D \sim 3.4 \pm 0.7$ nM) that are very similar to previous cell surface-binding studies showing that soluble NLGN2-Fc binds to HA-tagged MDGA1 expressed on COS7 cells with a K_D of ~ 7 nM (6), and also similar to fluorescence polarization studies where soluble ectodomains of MDGA1 WT and MDGA1 Ig1–Ig4 shown to bind NLGN2(+A) with K_D values of 48.4 ± 12.9 nM and 7.1 ± 2.5 nM, respectively (24). We implemented several technical improvements to the design of our SPR experiments (please see the [Experimental procedures](#) section) that may explain differences to prior SPR studies that either required a more difficult-to-evaluate binding model (2:1) compared with the one we used here (1:1) to fit the data to yield nanomolar binding affinity (25) or that determined ~ 1000 -fold weaker (micromolar) binding between pairs of proteins (8). Our mutants work as valuable

probes, with the disulfide bond $T^{333}C/Y^{519}C$ (Ig4–Ig5 elbow) directly validated by MS, whereas the presence of the disulfide bond $T^{135}C/N^{313}C$ (Ig2–Ig3 elbow) can be inferred based on similar SEC and NS-EM profiles compared with MDGA1 $T^{333}C/Y^{519}C$. Also, burying a charged residue in the Ig2–Ig3 or Ig4–Ig5 elbows, respectively, unambiguously shifts the molecular distribution to more open forms as seen by SEC and NS-EM. Taken together, our data suggest that the pronounced functional consequences of the designer mutants are because of neither rearrangements at the MDGA1–NLGN2 interaction site nor the local region around each mutation site but rather are due to the global impacts of the mutations, as discussed later.

Structure–function of the MDGA1 Ig2–Ig3 elbow

The Ig2–Ig3 elbow in MDGA1 is remarkable because of its sharp angle that is seen in three crystal structures (8, 25). It connects the binding site for NLGNs housed on the rigid tandem Ig1–Ig2 to the rest of the molecule (8, 24, 25). Despite its proximity to the NLGN interaction site on MDGA1, Ig3 is still about 15 Å away from NLGN1/NLGN2 (8, 25). Thus, our mutants targeting the Ig2–Ig3 elbow would not be expected to affect the structure of the NLGN2-binding site or its affinity, regardless of whether they exert a stabilizing (MDGA1 $T^{135}C/$

N³¹³C) or destabilizing (MDGA1 V³¹⁴D) effect on the respective hinge region. Indeed, the binding affinities of the purified soluble mutants for NLGN2(+A) are similar compared with MDGA1 WT (Fig. 7). Strikingly, locking the Ig2–Ig3 elbow (MDGA1 T¹³⁵C/N³¹³C) renders MDGA1 completely unable to bind NLGN2(+A) when it is tethered to the cell surface, but the non-membrane-bound form still binds NLGN2(+A) normally (Figs. 5 and 8). By contrast, promoting an open Ig2–Ig3 elbow (MDGA1 V³¹⁴D), which should facilitate access to the MDGA1 Ig1–Ig2 tandem, causes a near total loss of NLGN2 binding regardless of whether it is tethered or soluble in our cell surface-binding assays (Figs. 5 and 8). Also, altering the shape of MDGA1 *via* its Ig2–Ig3 elbow strongly decreases its biological function (little blocking of NLGN2 from NRXN1 β and no suppression of GABAergic presynaptic differentiation), despite the NLGN2 interaction site on the MDGA1 Ig1–Ig2 tandem being physically intact (Figs. 6 and 8). Thus, the Ig2–Ig3 elbow can critically control the 3D conformation of the MDGA1 molecule and its biological function.

Structure–function of the MDGA1 Ig4–Ig5 elbow

Mutants at the Ig4–Ig5 elbow either promoting the compact (T³³³C/Y⁵¹⁹C) or the extended (I³³⁶D) molecular conformations would not be expected to alter NLGN binding if the MDGA1 Ig1–Ig2 tandem functions independently from the rest of the molecule. Indeed, our SPR studies reveal that these purified soluble mutants bind NLGN2(+A) very similarly compared with MDGA1 WT suggesting that their binding interactions are preserved (Figs. 7 and 8). However, T³³³C/Y⁵¹⁹C, which locks the Ig4–Ig5 elbow, suppresses binding to NLGN2(+A) significantly when it is tethered to the cell surface but less so when it is soluble (Figs. 5 and 8), and it strongly impairs physiological function in biological assays, just like the MDGA1 T¹³⁵C/N³¹³C mutations in Ig2–Ig3 (Figs. 6 and 8). By contrast, I³³⁶D, which opens the Ig4–Ig5 elbow and is predicted to facilitate access to the MDGA1 Ig1–Ig2 tandem, strongly increases the amount of NLGN2 recruited to the surface, regardless of whether this mutant is tethered or soluble, though in biological assays, it appears roughly as active as MDGA1 WT (Figs. 5, 6 and 8). Our data are consistent with previous studies that were puzzling at the time, namely that removing the Ig4–Ig6 domains from MDGA1 (MDGA1 Δ Ig4–Ig6) doubled the amount of soluble NLGN2-Fc bound, whereas expressing just the Ig1–Ig3 domains (MDGA1 Ig1–Ig3) increased binding to NLGN2-Fc as well (though not as much) compared with MDGA1 WT tethered to the cell surface (6). Also, despite that MDGA1 Δ Ig4–Ig6 and MDGA1 Ig1–Ig3 bound more NLGN2 compared with MDGA1 WT at the cell surface, in those neuron-fibroblast assays neither truncation mutant suppressed synapse formation more efficiently either (6). It is possible that MDGAs engage additional proteins or that processes exist that are limiting in our biological assays so that the biological activity does not correspond proportionally with the amount of NLGN2 recruited on the cell surface for mutants like MDGA1

I³³⁶D. Nevertheless, our data show that the native structure of the Ig4–Ig5 elbow, like that of the Ig2–Ig3 elbow, is critical for the biological function of MDGA1.

Full-length MDGA1 structure–function relationships

Our mutants suggest that the overall 3D conformation of MDGA1 strategically orients the NLGN2-binding site located on Ig1–Ig2 with respect to the rest of the molecule, and thus that the NLGN2 interaction site on MDGA1 Ig1–Ig2 is not independent of the rest of the molecule. As a consequence, its exact placement within the synaptic cleft alters its function and renders it sensitive to the tethering status of MDGA1 on the presynaptic *versus* postsynaptic membrane (Fig. 8). In support, the detrimental effects of the mutants T¹³⁵C/N³¹³C (Ig2–Ig3) and T³³³C/Y⁵¹⁹C (Ig4–Ig5) are relieved when they are presented as soluble ectodomains, highlighting how finely tuned their steric fit and presentation are. Also, previous studies showed that NLGN2 and full-length MDGA1 when tethered on separate cell surfaces and presented *in trans* cannot interact (5), but when MDGA1 Ig1–Ig2 is presented as part of the small fragment Ig1–Ig3, *in trans* binding to NLGN2 is possible (25). If MDGA1 ectodomains were to behave like beads on a string, they would bind NLGN2 similarly well, regardless of whether they were tethered *in cis* or *in trans* or even presented in a soluble form. We thus conclude that MDGA1 function requires both the proper molecular shape of the ectodomain and also the appropriate tethering to the postsynaptic membrane to access and strategically position partner binding sites within the synaptic cleft.

Future work

Important questions remain. (1) How are MDGA molecules positioned in different synaptic clefts? MDGA1 molecules are ~140 Å long in the compact form and ~300 Å in the fully extended form by NS-EM. The width of synaptic clefts for excitatory synapses is estimated to be about 160 to 240 Å and that of inhibitory synapses is about 100 to 120 Å, based on microscopy (31–35). Thus, in the compact form, MDGA1 molecules bound to NLGN2 would fit very snugly in inhibitory synaptic clefts. This raises the question of whether MDGAs at the significantly wider excitatory synapses would be accommodated differently. (2) Could elongated and compact forms of MDGA1 coexist in a synaptic cleft, potentially dynamically interchanging, and/or carrying out different functions? It was noted that in the triangular form, MDGA1 domains Ig3 and Ig4 might prevent heparan sulfate moieties attached to NRXNs from binding to the deep cleft at the NLGN dimer interface and thus prevent their ability to promote NRXN–NLGN interaction (1, 36). Also, the high sequence conservation on the surface of the Ig4 domain that points inward toward the cleft at the NLGN2 dimer interface (Fig. 1E) suggests that yet unidentified partners may exist that bind MDGA1 alone or as part of a complex with NLGNs. Indeed, the MDGA1 MAM domain was recently shown to bind a novel partner, amyloid precursor protein, regulating synaptic inhibition in dendritic hippocampal CA1 pyramidal

neurons (37). Thus, other novel partners might also exist that selectively bind compact or elongated MDGA forms or shift the equilibrium between MDGA1 shapes. (3) Many missense mutations in MDGA1 have been found not only in humans with a diagnosis of SZ (<https://schema.broadinstitute.org>) but also in control cases. To what extent do missense mutations in MDGA1 result in proteins that carry an increased risk for neuropsychiatric disease? And do these mutations localize to strategic places in the protein structure, for example, at the molecular hinges, to alter function? For example, at the MDGA1 Ig2–Ig3 elbow F²³¹S and G²⁶⁷D, as well as at the MDGA1 Ig4–Ig5 elbow T⁴³⁷I and N⁵²³T would all be expected to destabilize the interface at the respective elbows and would be predicted to alter biological function based on our studies. Predicting whether other elbows could be equally functionally sensitive to mutations is more difficult. Some elbows involve only moderately sized buried surfaces, like Ig1–Ig2 (~640 Å², though stabilized through an intrinsic disulfide bond), Ig2–Ig3 (~650 Å²), Ig3–Ig4 (~560 Å²), and the very limited Ig5–Ig6 (~250 Å²), whereas very extensive interfaces are present for Ig4–Ig5 (~1000 Å²) and Ig6–FN3 (~1640 Å²) in the crystal structure (PDB ID: 5OJ2). The buried surface between the Ig1 and FN3 domains is also limited, only ~480 Å², but the arrangement of the other domains (in particular through the Ig4–Ig5 elbow) could force Ig1 and FN3 to maintain close proximity. Thus, the impact of missense mutations located at hinge regions as well as elsewhere in the MDGA1 protein will need to be experimentally assessed in terms of 3D structure, function, and disease burden. (4) What is the molecular basis of the proposed selectivity code for interactions between MDGAs and NLGNs? MDGA1 appears to selectively regulate NLGN2 impacting inhibitory synaptic transmission, whereas MDGA2 ultimately impacts NLGN1 and excitatory synapses more though it can interact with both NLGN1 and NLGN2 (5–7, 9). Cell-based studies have shown that MDGA1 on the cell surface binds to soluble NLGN2 ectodomain with greater affinity ($K_D \sim 7$ nM) than MDGA2 ($K_D \sim 46$ nM) and that MDGA2 binds to NLGN1(+B) and can accommodate site B, whereas MDGA1 cannot (6). However, the exact selectivity between MDGAs and NLGNs remains unclear, and its molecular basis as well (8, 13, 14). (5) Could splicing of NLGNs synergize with the 3D conformational state of MDGAs and its fit in the synaptic cleft to regulate binding? We and others have previously shown that the site B insert in NLGN1 strongly decreases binding to MDGA1 likely because of steric clashes (5, 6, 8, 24). By contrast, site A in NLGN2 does not seem to impact binding, at least for MDGA1 molecules tethered to the cell surface (Fig. 5) in agreement with previous studies (5).

Our work here demonstrating the ability of MDGA1 molecules to adopt a range of conformations *in vitro* (spanning compact to elongated forms) and their exquisite functional sensitivity to 3D shape and orientation is an important step forward because it suggests that the 3D shape of MDGA1 may act as a molecular sensor to regulate protein partner interactions. It will be important to assess the impact of our mutants in other biologically relevant settings, for example,

leveraging electrophysiology or generating knock-in mice, to assess the full scope of MDGA1 structure–function relationships *in vivo*. Finally, given the genetic linkage of MDGA1 to several neuropsychiatric disorders including autism spectrum disorders and SZ (9, 38, 39), our designer mutants may also serve as important tools to test whether manipulating MDGA1 (and analogously MDGA2) can be used to selectively regulate inhibitory *versus* excitatory synapse development/stabilization, the imbalance of which is associated with severe behavioral dysfunction in many neuropsychiatric disorders (7, 40, 41) or to engineer unique synaptic connectivities to ameliorate disrupted neural circuits such as those seen in neuropsychiatric disorders.

Experimental procedures

Methods

Protein expression and purification

Human MDGA1 (corresponding to GenBank accession number: NM_153487), residue range 22 to 920 (lacking the GPI anchor region), or mutants were cloned with a C-terminal ASTSHHHHHH tag in the pFastbac vector. The construct also contains the N-terminal residues ELGTGVD and the C-terminal residues GS from the cloning linkers. The proteins were produced using baculovirus-mediated overexpression in High Five cells (Thermo Fisher; catalog no.: B85502) grown in ExCell 405/L-glutamine medium (MilliporeSigma; catalog no.: 14405C) supplemented with L-glutamine (Gibco; catalog no.: 25030081) and an antibiotic–antimycotic solution (Gibco; catalog no.: 15240096) at 28 °C for 72 h. The following proteins were produced: human MDGA1 WT and its mutants MDGA1 T¹³⁵C/N³¹³C, MDGA1 V³¹⁴D, MDGA1 T³³³C/Y⁵¹⁹C, and MDGA1 I³³⁶D, and rat NLGN2(+A). For MDGA1 WT, medium containing the overexpressed and secreted protein was supplemented with protease inhibitors (pepstatin, leupeptin, and PMSF), concentrated, dialyzed overnight against 25 mM sodium phosphate, pH 8.0, 500 mM NaCl, and subjected to affinity chromatography at 4 °C using a nickel–nitrilotriacetic acid column (Invitrogen) equilibrated with 25 mM sodium phosphate, pH 8, 500 mM NaCl. Bound protein was eluted with an imidazole gradient in the same buffer. Subsequently, the protein was dialyzed in 10 mM Hepes, 150 mM NaCl, pH 8, and then subjected to SEC using a HiLoad Superdex-200 16/60 column (GE Healthcare) equilibrated with 10 mM Hepes, 150 mM NaCl, pH 8. For MDGA1 T¹³⁵C/N³¹³C, MDGA1 V³¹⁴D, MDGA1 T³³³C/Y⁵¹⁹C, and MDGA1 I³³⁶D, the proteins were similarly purified using a nickel–nitrilotriacetic acid column, dialyzed against 20 mM Hepes, pH 7.3, 50 mM NaCl, 2% (v/v) glycerol overnight, and then subjected to cation exchange chromatography using a Mono S column (GE Healthcare) in 20 mM Hepes, pH 7.3, 50 mM NaCl, 2% (v/v) glycerol, and eluted with a NaCl gradient. All purified proteins were concentrated, aliquoted, flash-frozen in liquid nitrogen, and stored at –80 °C until use. The mutations were verified by tryptic peptide mapping using MS. Yields for MDGA1 T¹³⁵C/N³¹³C, MDGA1 V³¹⁴D, MDGA1 T³³³C/Y⁵¹⁹C, and MDGA1 I³³⁶D were significantly reduced compared with WT, which precluded AUC

experiments. The extracellular domain of rat NLGN2 (GenBank accession number: NM_053992; residues V43–H612) with splice insert A (amino acids GPLTKKRDEATLNPPDT, NLGN2(+A)) was generated and purified as previously described (24). Mws and purity of all proteins were evaluated by SDS-PAGE and MS.

Analytical SEC

Proteins MDGA1 WT (1.43 mg/ml), MDGA1 T¹³⁵C/N³¹³C (0.275 mg/ml), MDGA1 V³¹⁴D (0.275 mg/ml), MDGA1 T³³³C/Y⁵¹⁹C (0.275 mg/ml), and MDGA1 I³³⁶D (0.275 mg/ml) were dialyzed for 6 h in low-ionic strength (LS) buffer (10 mM Hepes, 50 mM NaCl, pH 8) or high-ionic strength (HS) buffer (10 mM Hepes, 500 mM NaCl, pH 8). Samples were centrifuged at 13,000 rpm at 4 °C to remove any nonsoluble matter and then applied in a 20 µl volume to an analytical SEC column (Superdex 200 Increase 3.2/300; GE Healthcare) equilibrated with the respective LS or HS buffer at a flow rate of 0.02 ml/min at 4 °C. The column was calibrated with three Mw standards, β-amylase (200,000 Da), albumin (66,000 Da), and cytochrome *c* (12,900 Da) (Sigma) in LS or HS buffer, respectively. All samples were run in triplicate to obtain averages and SDs.

AUC

Sedimentation velocity AUC experiments were performed using a Beckman Coulter Model XL-A analytical ultracentrifuge in 12 mm double sector (2-channel) cells with quartz windows and an An-60 Ti rotor at 42,000 rpm (141,995 RCF) at 20 °C. Prior to experiments, MDGA1 WT samples were dialyzed at 20 °C for 12 h against ~1000-fold excess of 10 mM Hepes, 50 mM NaCl, pH 8 or 10 mM Hepes, 500 mM NaCl, pH 8, respectively. The dialysate was used as the reference solution. Samples were filtered using Amicon Ultra spin filters (catalog no.: UFC500324) and brought to a concentration of 1.2 mg/ml with the relevant buffer (giving an absorbance of ~0.8 at 280 nm) in a volume of 400 µl. Protein concentrations were measured with a DeNovix DS-11+ spectrophotometer using a calculated extinction coefficient of 112,650 M⁻¹ cm⁻¹ (42). Prior to sedimentation experiments, samples were centrifuged for 10 min at 13,000 rpm at 4 °C to remove any particulate matter from the bulk solution. Absorbance scans of the cells were recorded at 280 nm every 2 min with a step size of 0.003 cm. Solvent density and viscosity, as well as estimates of the partial specific volume of MDGA1 WT at 20 °C, were calculated using SEDNTERP (43). Analysis of the AUC data was carried out with SEDFIT, version 16.2 (44) using the continuous sedimentation coefficient distribution model. Calculation of standardized sedimentation coefficients (*S*_{w,20}) and generation of high-resolution plots were performed using SEDFIT, version 16.2 and Gussi 1.4.2, respectively (44, 45).

Multisequence alignment of MDGA1

MDGA1 sequences from 212 higher organisms (aves, mammalia, amphibia, crocodylia, lepidosauria, and

testudinoidea; Table S2) were used to generate a multi-sequence alignment using the MUSCLE program (46).

Analysis of the 3D structure of MDGA1

The solvent-accessible surface of chicken MDGA1 was analyzed with the PISA program (47) using coordinates of the X-ray crystal structure of the MDGA1–NLGN1 complex (PDB ID: 5OJ6; (8)).

Mutant modeling

MDGA1 mutants were designed by visual inspection of the crystal structure of MDGA1 (PDB ID: 5OJ2) using the Coot program (48). To favor compact MDGA1 conformations, we introduced one disulfide bond each across the Ig2–Ig3 and I4–Ig5 elbows, respectively, by selecting one residue each on either side of the connecting regions whose mutation to cysteine would place the S_γ atoms at a distance that supports disulfide-bond formation while avoiding unfavorable rotameric conformations. To favor less compact MDGA1 conformations, we replaced a hydrophobic residue with an aspartate residue in the cores of the interfaces of the Ig2–Ig3 and Ig4–Ig5 elbows, respectively, to destabilize the interfaces by burying a negative charge. Prior to designing the mutants, we made the following two modifications to the published coordinates, both of which are compatible with the published electron density: (a) we modeled the Q³³⁵ side chain with the terminal group flipped in both molecules in the asymmetric unit to maximize hydrogen bonding and (b) we modeled the side chain of I⁵²³ in molecule A with that used in molecule B to alleviate significant steric clashes.

SPR

Binding of MDGA1 proteins to NLGN2(+A) was assessed in SPR buffer (10 mM Hepes, 150 mM NaCl, pH 7.4, 0.1% [v/v] Tween-20) at 25 °C with a Biacore T100 system. C1 sensor chips, which lack a dextran matrix, were chosen to reduce nonspecific binding and avoid the need for blocking agents in the running buffer, as well as to ensure sparsely populated ligand surfaces. MDGA1 WT (*M*_w ~112 kDa) and mutants were immobilized on C1 sensor chips (Cytiva) using amine-coupling chemistry by activating all flow cells in the chip with a 1:5 mixture of ~0.1 M *N*-hydroxysuccinimide and ~0.5 M 3-(*N,N*-dimethylamino)propyl-*N*-ethylcarbodiimide for 7 min with a flow rate of 10 µl/min (see Figs. 7 and S6 for immobilization levels). Binding data were obtained by injecting a concentration series of NLGN2(+A) (*M*_{w,dimer} = 135.7 kDa) over sensors with and without MDGA1 coupled and analyzing the differences in response units. NLGN2(+A) dimers were flowed over the chip with concentrations of 2.81, 5.63, 11.25, 22.5, 45, and 90 nM, respectively, with a flow rate of 30 µl/min for 120 s (association step) followed by SPR buffer only for 120 s (dissociation step). Sensors were regenerated after each protein injection with a total of 400 µl regeneration buffer (3 mM NaOH, 500 mM NaCl; at 100 µl/min). Data were processed using a kinetic analysis. The sensorgram data were fitted using an *R*_{max} local fitting method to a model describing a 1:1 bimolecular association reaction between an MDGA1

monomer immobilized on the chip and the soluble NLGN2 dimer. Each experiment was carried out in duplicate on the same chip. Subsequently, each experiment was repeated on a different C1 sensor chip to generate a second set of independent experiments. The final reported values of the kinetic association and dissociation constants k_a and k_d and the derived equilibrium binding constant K_D were obtained by calculating the average values and SD for all runs in each experiment (as shown in the plots in Fig. S7) and together for all experiments (as shown in the table in Fig. 7).

NS-EM

Sample preparation—MDGAs dialyzed against 10 mM Hepes, 50 mM NaCl, pH 8 were diluted to 4 μ g/ml. MDGA1 WT was diluted in LS buffer (10 mM Hepes, 50 mM NaCl, pH 8) or HS buffer (10 mM Hepes, 500 mM NaCl, pH 8), whereas the mutants (MDGA1 T¹³⁵C/N³¹³C, MDGA1 V³¹⁴D, MDGA1 T³³³C/Y⁵¹⁹C, and MDGA1 I³³⁶D) were diluted in HS buffer only. MDGA1 and NLGN2 (+A) were mixed and diluted in LS buffer with 3 mM CaCl₂ added. Protein amounts were adjusted empirically to give roughly equal representations of the particles on the EM grids to avoid bias because of differences in the imaging qualities of the various particles. Specimens were prepared as previously described (49, 50). Briefly, an aliquot (4 μ l) of the sample solution was placed on an ultrathin carbon continuous film grid (CF-200-Cu-UL; Electron Microscopy Sciences) that was glow-discharged for 15 s. After 1 min incubation, excess solution on the grid was removed using filter paper. The grid was then stained with three drops of 1% (w/v) uranyl formate. The excess solution on the grid was again removed with filter paper by blotting from the rear side, and the grid was then immediately dried with nitrogen.

EM data acquisition and reference-free 2D class averaging—The NS-EM specimens were examined using a Zeiss Libra 120 Plus TEM (Carl Zeiss NTS). The instrument was equipped with an LaB6 gun operating at 120 kV, an in-column energy filter, and a 4 k \times 4 k Gatan UltraScan 4000 charge-coupled device camera. The micrographs were acquired under near Scherzer defocus at a magnification of 80,000 \times (corresponding to 1.48 \AA /pixel). For 2D reference-free class averaging analysis, particles were selected from the micrographs that were low-pass filtered to 15 \AA after X-ray speckles were removed and then subjected to reference-free class averaging with the EMAN (Electron Micrograph ANalysis, Baylor College of Medicine, TX) program (51). The number of micrographs, particles, and classes for each sample are listed in Table S1.

Electron tomography data acquisition and IPET 3D reconstruction

MDGA1 WT in HS buffer was used as a representative sample to study the structural flexibility of MDGA1. A total of six tilt series of ET data were collected at a magnification of 80,000 \times (corresponding to 1.48 \AA /pixel) under defocus of \sim 0.6 μ m using Gatan tomography software and in-house developed fully mechanically controlled automated electron tomography software (52). The tilting range was from -48° to $+48^\circ$ in 1.5° increments.

The tilt series of whole micrographs were initially aligned by IMOD (version 4.11, the University of Colorado) (53). The contrast transfer function was determined by the GCTF software package and then corrected by TOMOCTF (54). In addition, a contrast enhancement method was applied to reduce the image noise (55). For IPET reconstructions, seven representative MDGA1 molecules were selected to represent the diversity of observed shapes; IPET permits flexible molecules to be 3D reconstructed using a series of 3D maps from a single molecule without averaging (30). Briefly, a 256 \times 256-pixel tilt series containing MDGA1 molecule was selected from the whole micrograph tilt series and then back-projected to generate an *ab initio* 3D map as an initial model. After iteration and refinement processes, the generated 3D map was submitted to a low-tilt tomographic 3D reconstruction method (LoTTorR) to reduce the missing-wedge artifact caused by the limited tilt angle range (56). Finally, seven IPET 3D maps with representative conformations of MDGA1 were low-pass filtered to 40 \AA and rendered in UCSF Chimera (57).

Statistics

Particle Shape Distribution—To quantify the size of different particles from the different MDGA1 proteins, we selected five typical micrographs from every sample and picked all isolated particles to avoid sampling bias (Table S1). To characterize compact *versus* more elongated conformations, we measured two perpendicular directions for each particle, cataloging the long distance and short distances (Fig. 4I). We then calculated the ratios of long *versus* short distances and also the polygon area of four points defined for each particle analyzed.

DNA constructs for cell-based studies

The following constructs were used for cell-based assays and have previously been described: HA-tagged rat MDGA1 (complete mature protein [residues 19–956] with N-terminal HA tag; (6)) and HA-tagged extracellular region of CD4 (HA-CD4) (6, 58). Novel constructs were generated for MDGA1 mutants by site-directed mutagenesis using HA-tagged rat MDGA1 as the template. The following constructs were gifts from Peter Scheiffele: pNICE-NLGN2(+A) (Addgene: Plasmid #15259) and pNICE-NLGN2(-A) (Addgene: Plasmid #15246). For Myc-NLGN2(+A), the mature form of NLGN2 was amplified by PCR using pNICE-NLGN2(+A) (Addgene: Plasmid #15259) as a template and then subcloned into spTrkC-Myc-C1, a vector that expresses Myc with an N-terminal signal sequence derived from TrkC. To generate the human Ig Fc-fusion NLGN2 proteins NLGN2(+A)-Fc and NLGN2(-A)-Fc, the mature ectodomain of mouse NLGN2 was amplified by PCR using pNICE-NLGN2(+A) and pNICE-NLGN2(-A), respectively and then subcloned in the pcDNA4-spNRX1 β -Fc vector (59). All constructs were verified by DNA sequencing.

In situ cell surface binding assay using soluble Fc-fusion and (His)₆-tagged proteins

Purified soluble recombinant human NRXN1 β (-SS4) ectodomain fused to the human Ig Fc domain (NRXN1 β (-SS4)-Fc)

was purchased from R&D Systems (catalog no.: 5268-NX-050). To produce soluble NLGN2-Fc proteins, NLGN2-Fc-expressing plasmids were transfected into HEK293T cells using TransIT-PRO (Mirus Bio LLC; catalog number: MIR5740) and cultured in Dulbecco's modified Eagle's medium (DMEM) (Gibco; catalog number: 11965118) containing 10% (v/v) fetal bovine serum (FBS) (Wisent; catalog number: 080-150). At 24 h after transfection, the medium was replaced with serum-free AIM V synthetic medium (Gibco; catalog number: 12055083). The conditioned medium was collected after 5 days, and NLGN2-Fc protein concentration was measured by Western blot using purified human IgG as a standard. Protein binding assays were performed as described previously (60). Briefly, to assess protein binding on the surface of COS7 cells, plasmids encoding target proteins fused to extracellular HA tags or Myc tags were transfected into COS7 cells using TransIT-LT1 (Mirus Bio. LLC; catalog number: MIR2305) and cultured in DMEM containing 10% (v/v) FBS. At 24 h after transfection, the transfected COS7 cells were washed with extracellular solution (ECS: 168 mM NaCl, 2.4 mM KCl, 20 mM Hepes, pH 7.4, 10 mM D-glucose, 2 mM CaCl₂, and 1.3 mM MgCl₂) with 100 µg/ml bovine serum albumin (BSA; Sigma, catalog number: A9647) added; the cells were then incubated for 1 h at 4 °C with ECS + BSA containing the appropriate Fc-fusion or (His)₆-tagged protein. The following protein concentrations were applied to transfected COS7 cells: 50 nM for NLGN2(+A)-Fc and NLGN2(-A)-Fc, 200 nM for (His)₆-tagged MDGA1 WT or MDGA1 mutants, and 100 nM for NRXN1β(-SS4)-Fc. Cells were washed with ECS and subsequently fixed in prewarmed 4% (v/v) formaldehyde/4% (w/v) sucrose for 12 min and blocked in 5% (v/v) normal donkey serum/3% (w/v) BSA in PBS for 1 h at room temperature. Cells were incubated with anti-HA (1:2000 dilution; from rabbit; Abcam, catalog number: ab9110), anti-HA (1:1000 dilution; rat; catalog no.: 11867423001; Roche, catalog number: ROA-HAHA), anti-6xHIS (1:1000 dilution; rabbit; Abcam, catalog number: ab213204) and anti-Myc (1:1000 dilution; mouse; sc-40; Santa Cruz Biotechnology, catalog number: sc-40) without permeabilization overnight at 4 °C. Cells were then incubated with highly cross-adsorbed Alexa dye-conjugated secondary antibodies generated in donkey toward the appropriate species (1:500 dilution; Jackson ImmunoResearch).

Artificial synapse formation assay

Rat hippocampal neuron cultures and coculture of hippocampal neurons with HEK293T cells for performing artificial synapse formation assays were carried out as described previously (59). All animal experiments were carried out in accordance with the Canadian Council on Animal Care guidelines and approved by the Institut de recherches cliniques de Montréal (IRCM) Animal Care Committee. Briefly, hippocampal neurons from E18 rat embryos were cultured at high density on poly-L-lysine-coated glass coverslips in neurobasal medium (Gibco; catalog number: 21103-049) supplemented with NeuroCult SM1 (StemCell; catalog number: 05711) and GlutaMaX (Gibco; catalog number: 35050061). For neuron-

HEK293T coculture assays, Myc-NLGN2(+A) with HA-MDGA1, HA-MDGA1 mutants, or HA-CD4 were cotransfected at an equal DNA ratio in HEK293T cells using TransIT-LT1 (Mirus Bio. LLC; catalog number: MIR2305) and cultured in DMEM containing 10% (v/v) FBS. At 24 h after transfection, cells were harvested by trypsinization and seeded on the neuronal growth surface. After 24 h of coculture, cells were fixed in prewarmed 4% (v/v) formaldehyde/4% (w/v) sucrose for 12 min and blocked with 5% (v/v) normal donkey serum /3% (w/v) BSA in PBS for 1 h at room temperature. Cells were incubated with anti-HA (1:1000 dilution; rat, catalog no.: 11867423001; Roche, catalog number: ROA-HAHA) and anti-Myc (1:1000 dilution; mouse; sc-40; Santa Cruz Biotechnology, catalog number: sc-40) overnight at 4 °C to label surface MDGA1 WT, MDGA1 mutants, CD4, or NLGN2(+A) respectively. Cells were then permeabilized in 0.2% (v/v) Triton X-100 in PBS and incubated with anti-VGAT (1:500 dilution; rabbit; catalog no.: 131003; Synaptic Systems, catalog number: 131003) overnight at 4 °C to label intracellular VGAT. Cells were then incubated with highly cross-adsorbed Alexa dye-conjugated secondary antibodies generated in donkey toward the appropriate species (1:500 dilution; Jackson ImmunoResearch).

Imaging of cell-based assays

Images were acquired on a Leica DM6000 fluorescence microscope with a 40 × 0.75 numerical aperture dry objective and 63 × 1.4 numerical aperture oil objective for *in situ* binding and artificial synapse formation assays, respectively, with a Hamamatsu cooled charge-coupled device camera using the Volocity software (PerkinElmer). Images were acquired as 12 bit grayscale and prepared for presentation using Adobe Photoshop CS2. For quantification, sets of cells were fixed and stained simultaneously and imaged with identical settings. All image acquisitions, analyses, and quantifications were performed by investigators blind to the experimental condition.

Image analysis and statistical analyses of cell-based assays

To quantify binding levels and cell surface expression levels, we measured the average intensity of each channel within the delineated COS7 or HEK293T cell area subtracted by the average intensity of the off-cell background. For *in situ* binding assays, the average intensity of bound NLGN2-Fc proteins was normalized using the average surface intensity for HA-MDGA1, HA-MDGA1 mutants, or HA-CD4. The average intensity of bound (His)₆-tagged MDGA1 proteins was normalized using the average surface intensity of HA-NLGN2(+A). The average intensity of bound NRXN1β-Fc was normalized using the average surface intensity of Myc-NLGN2(+A). COS7 cells expressing similar levels of HA- and Myc-tagged proteins were selected to quantify bound NRXN1β-Fc. Analyses were performed using Volocity 6.0, Excel for Microsoft 365 (Microsoft), and Prism 9 (GraphPad Software, Inc). For the artificial synapse formation assays, HEK293T cells displaying similar surface levels of NLGN2(+A) and MDGA1 WT or mutants or CD4 were

imaged without considering the other fluorescence channels. To assess NLGN2-mediated GABAergic presynaptic differentiation, the fluorescence channel corresponding to VGAT was thresholded and the total intensity of puncta within all regions positive for both surface HA (labeling MDGA1 WT, MDGA1 mutants, or CD4) and Myc (labeling NLGN2(+A)) was measured. Analysis was performed using Metamorph 7.8 (Molecular Devices), Excel 2003, and Prism 9. Bartlett's tests were performed to assess whether SDs were significantly different across conditions. Statistical comparisons were made using one-way ANOVA or Welch's ANOVA with Dunnett's T3 multiple comparisons tests, as indicated in the figure legends. All data are reported as the mean \pm SEM from three independent experiments, and statistical significance was defined as $p < 0.05$.

Data availability

All data are contained within the article.

Supporting information—This article contains supporting information (references (61–64)).

Acknowledgments—Dr Luis Holthauzen (The University of Texas Medical Branch, Galveston, TX, USA) and Dr Chad Brautigam (The University of Texas Southwestern Medical Center, Dallas, TX, USA) are sincerely thanked for insightful discussions about SPR and AUC; Dr Shanti Pal Gangwar is thanked for insightful discussions regarding the MDGA1 3D structure. Dr Zhuoyang Lu gratefully acknowledges support and guidance from Prof Jiankang Liu at the School of Life Science and Technology and Frontier Institute of Science and Technology, Xi'an Jiaotong University, Xi'an, China.

Author contributions—G. R., H. T., and Gab. R. conceptualization; H. L., N. C., J. L., S. F., Z. L., M. R. R., P. P., A. O. B., W. K. R., M. M., G. R., H. T., and Gab. R. validation; H. L., N. C., J. L., A. O. B., M. M., Gab. R. formal analysis; H. L., N. C., J. L., S. F., Z. L., M. R. R., P. P., A. O. B., and M. M. investigation; H. L. and Gab. R. writing—original draft; H. L., N. C., J. L., S. F., Z. L., M. R. R., P. P., A. O. B., W. K. R., M. M., G. R., H. T., and Gab. R. writing—review & editing; H. L., N. C., J. L., M. M., Gab. R. visualization; Gab. R. supervision; G. R., H. T., and Gab. R. project administration; G. R., H. T., and Gab. R. funding acquisition.

Funding and additional information—This work was funded by National Institute of Mental Health (grant no.: R01MH077303), the Sealy Center for Structural Biology and Molecular Biophysics at The University of Texas Medical Branch (UTMB), Galveston, TX, USA (to G. R.) and supported by the Canadian Institutes of Health Research grant (grant no.: MOP-133517), Natural Science and Engineering Research Council Discovery grant (grant no.: RGPIN-2017-04753), and a Fonds de la Recherche du Québec Research Scholars (senior) grant (to H. T.). H. L. was supported in part by the Jeane B. Kempner Fellowship Program, UTMB, and the UTMB Center for Addiction Research Predoctoral Fellowship (National Institute on Drug Abuse T32 grant DA 07287). The work at the Molecular Foundry, Lawrence Berkeley National Laboratory was supported by the Office of Science, Office of Basic Energy Sciences of the US Department of Energy (contract no. DE-AC02-05CH11231), and US National Institutes of Health grants R01HL115153, R01GM104427, R01MH077303, and R01DK042667

(to G. R. and J. L.). The MS facilities at UTMB are funded in part by the Cancer Prevention Research Institute of Texas (grant no.: RP190682; to W. R.).

Conflict of interest—The authors declare that they have no conflicts of interest with the contents of this article.

Abbreviations—The abbreviations used are: AUC, analytical ultracentrifugation; BSA, bovine serum albumin; DMEM, Dulbecco's modified Eagle's medium; ECS, extracellular solution; ET, electron tomography; EV, elution volume; FNIII, fibronectin III; GPI, glycosylphosphatidylinositol; HA, hemagglutinin; HEK293T, human embryonic kidney 293T cell line; HS, high salt; Ig, immunoglobulin; IPET, individual particle electron tomography; LS, low salt; MAM, meprin, A-5 protein, receptor protein-tyrosine phosphatase μ ; MDGA, MAM domain-containing glycosylphosphatidylinositol anchor; MS, mass spectrometry; Mw, molecular weight; NLGN, neuroligin; NRXN, neurexin; NS-EM, negative-staining EM; PDB, Protein Data Bank; SEC, size-exclusion chromatography; SPR, surface plasmon resonance; SZ, schizophrenia; UTMB, University of Texas Medical Branch; VGAT, vesicular GABA transporter.

References

1. Connor, S. A., Elegheert, J., Xie, Y., and Craig, A. M. (2019) Pumping the brakes: suppression of synapse development by MDGA-neuroligin interactions. *Curr. Opin. Neurobiol.* **57**, 71–80
2. Sudhof, T. C. (2017) Synaptic neurexin complexes: a molecular code for the logic of neural circuits. *Cell* **171**, 745–769
3. Gomez, A. M., Traunmuller, L., and Scheiffele, P. (2021) Neurexins: molecular codes for shaping neuronal synapses. *Nat. Rev. Neurosci.* **22**, 137–151
4. Kim, H. Y., Um, J. W., and Ko, J. (2021) Proper synaptic adhesion signaling in the control of neural circuit architecture and brain function. *Prog. Neurobiol.* **200**, 101983
5. Lee, K., Kim, Y., Lee, S.-J., Qiang, Y., Lee, D., Lee, H. W., *et al.* (2013) MDGAs interact selectively with neuroligin-2 but not other neuroligins to regulate inhibitory synapse development. *Proc. Natl. Acad. Sci. U. S. A.* **110**, 336–341
6. Pettem, K. L., Yokomaku, D., Takahashi, H., Ge, Y., and Craig, A. M. (2013) Interaction between autism-linked MDGAs and neuroligins suppresses inhibitory synapse development. *J. Cell Biol.* **200**, 321–336
7. Connor, S. A., Ammendrup-Johnsen, I., Chan, A. W., Kishimoto, Y., Murayama, C., Kurihara, N., *et al.* (2016) Altered cortical dynamics and cognitive function upon haploinsufficiency of the autism-linked excitatory synaptic suppressor MDGA2. *Neuron* **91**, 1052–1068
8. Elegheert, J., Cvetkovska, V., Clayton, A. J., Heroven, C., Vennekens, K. M., Smukowski, S. N., *et al.* (2017) Structural mechanism for modulation of synaptic neuroligin-neurexin signaling by MDGA proteins. *Neuron* **95**, 896–913.e10
9. Connor, S. A., Ammendrup-Johnsen, I., Kishimoto, Y., Karimi Tari, P., Cvetkovska, V., Harada, T., *et al.* (2017) Loss of synapse repressor MDGA1 enhances perisomatic inhibition, confers resistance to network excitation, and impairs cognitive function. *Cell Rep.* **21**, 3637–3645
10. Levinson, J. N., Chery, N., Huang, K., Wong, T. P., Gerrow, K., Kang, R., *et al.* (2005) Neuroligins mediate excitatory and inhibitory synapse formation: involvement of PSD-95 and neurexin-1beta in neuroligin-induced synaptic specificity. *J. Biol. Chem.* **280**, 17312–17319
11. Chubykin, A. A., Atasoy, D., Etherton, M. R., Brose, N., Kavalali, E. T., Gibson, J. R., *et al.* (2007) Activity-dependent validation of excitatory versus inhibitory synapses by neuroligin-1 versus neuroligin-2. *Neuron* **54**, 919–931
12. Varoqueaux, F., Jamain, S., and Brose, N. (2004) Neuroligin 2 is exclusively localized to inhibitory synapses. *Eur. J. Cell Biol.* **83**, 449–456
13. Toledo, A., Letellier, M., Bimbi, G., Tessier, B., Daburon, S., Favereaux, A., *et al.* (2022) MDGAs are fast-diffusing molecules that delay excitatory synapse development by altering neuroligin behavior. *Elife* **11**, e75233

14. Loh, K. H., Stawski, P. S., Draycott, A. S., Udeshi, N. D., Lehrman, E. K., Wilton, D. K., *et al.* (2016) Proteomic analysis of unbounded cellular compartments: synaptic clefts. *Cell* **166**, 1295–1307.e21
15. Fuccillo, M. V., and Pak, C. (2021) Copy number variants in neurexin genes: phenotypes and mechanisms. *Curr. Opin. Genet. Dev.* **68**, 64–70
16. Tromp, A., Mowry, B., and Giacomotto, J. (2021) Neurexins in autism and schizophrenia—a review of patient mutations, mouse models and potential future directions. *Mol. Psych.* **26**, 747–760
17. Cuttler, K., Hassan, M., Carr, J., Cloete, R., and Barden, S. (2021) Emerging evidence implicating a role for neurexins in neurodegenerative and neuropsychiatric disorders. *Open Biol.* **11**, 210091
18. Pohl, T. T., and Hornberg, H. (2022) Neuroligins in neurodevelopmental conditions: how mouse models of *de novo* mutations can help us link synaptic function to social behavior. *Neuronal Signal.* **6**, NS20210030
19. Taylor, S. C., Ferri, S. L., Grewal, M., Smernoff, Z., Bucan, M., Weiner, J. A., *et al.* (2020) The role of synaptic cell adhesion molecules and associated scaffolding proteins in social affiliative behaviors. *Biol. Psych.* **88**, 442–451
20. Lee, E., Lee, J., and Kim, E. (2017) Excitation/inhibition imbalance in animal models of autism spectrum disorders. *Biol. Psych.* **81**, 838–847
21. Rudenko, G. (2017) Dynamic control of synaptic adhesion and organizing molecules in synaptic plasticity. *Neural Plast.* **2017**, 6526151
22. Delorme, R., Ey, E., Toro, R., Leboyer, M., Gillberg, C., and Bourgeron, T. (2013) Progress toward treatments for synaptic defects in autism. *Nat. Med.* **19**, 685–694
23. Fan, S., Gangwar, S. P., Machius, M., and Rudenko, G. (2021) Interplay between hevin, SPARC, and MDGAs: modulators of neurexin-neuroligin transsynaptic bridges. *Structure* **29**, 664–678.e6
24. Gangwar, S. P., Zhong, X., Seshadrinathan, S., Chen, H., Machius, M., and Rudenko, G. (2017) Molecular mechanism of MDGA1: regulation of neuroligin 2:neurexin trans-synaptic bridges. *Neuron* **94**, 1132–1141.e4
25. Kim, J. A., Kim, D., Won, S. Y., Han, K. A., Park, D., Cho, E., *et al.* (2017) Structural insights into modulation of neurexin-neuroligin trans-synaptic adhesion by MDGA1/neuroligin-2 complex. *Neuron* **94**, 1121–1131.e6
26. Südhof, T. C. (2008) Neuroligins and neurexins link synaptic function to cognitive disease. *Nature* **455**, 903–911
27. Boucard, A. A., Chubykin, A. A., Comoletti, D., Taylor, P., and Südhof, T. C. (2005) A splice code for trans-synaptic cell adhesion mediated by binding of neuroligin 1 to alpha- and beta-neurexins. *Neuron* **48**, 229–236
28. Chih, B., Gollan, L., and Scheiffele, P. (2006) Alternative splicing controls selective trans-synaptic interactions of the neuroligin-neurexin complex. *Neuron* **51**, 171–178
29. Schreiner, D., Simicevic, J., Ahrne, E., Schmidt, A., and Scheiffele, P. (2015) Quantitative isoform-profiling of highly diversified recognition molecules. *Elife* **4**, e07794
30. Zhang, L., and Ren, G. (2012) IPET and FETR: experimental approach for studying molecular structure dynamics by cryo-electron tomography of a single-molecule structure. *PLoS one* **7**, e30249
31. Lucic, V., Yang, T., Schweikert, G., Forster, F., and Baumeister, W. (2005) Morphological characterization of molecular complexes present in the synaptic cleft. *Structure* **13**, 423–434
32. Zuber, B., Nikonenko, I., Klausner, P., Muller, D., and Dubochet, J. (2005) The mammalian central nervous synaptic cleft contains a high density of periodically organized complexes. *Proc. Natl. Acad. Sci. U. S. A.* **102**, 19192–19197
33. Harris, K. M., and Weinberg, R. J. (2012) Ultrastructure of synapses in the mammalian brain. *Cold Spring Harb. Perspect. Biol.* **4**, a005587
34. Perez de Arce, K., Schrod, N., Metzbowser, S. W. R., Allgeyer, E., Kong, G. K.-W., Tang, A.-H., *et al.* (2015) Topographic mapping of the synaptic cleft into adhesive nanodomains. *Neuron* **88**, 1165–1172
35. High, B., Cole, A. A., Chen, X., and Reese, T. S. (2015) Electron microscopic tomography reveals discrete trans-cleft elements at excitatory and inhibitory synapses. *Front. Synaptic Neurosci.* **7**, 9
36. Oku, S., Feng, H., Connor, S., Toledo, A., Zhang, P., Zhang, Y., *et al.* (2020) Alternative splicing at neuroligin site A regulates glycan interaction and synaptogenic activity. *Elife* **9**, e58668
37. Kim, J., Kim, S., Kim, H., Hwang, I. W., Bae, S., Karki, S., *et al.* (2022) MDGA1 negatively regulates amyloid precursor protein-mediated synapse inhibition in the hippocampus. *Proc. Natl. Acad. Sci. U. S. A.* **119**, e2115326119
38. Wang, R., Dong, J. X., Wang, L., Dong, X. Y., Anenberg, E., Jiang, P. F., *et al.* (2019) A negative regulator of synaptic development: MDGA and its links to neurodevelopmental disorders. *World J. Pediatr.* **15**, 415–421
39. Li, J., Liu, J., Feng, G., Li, T., Zhao, Q., Li, Y., *et al.* (2011) The MDGA1 gene confers risk to schizophrenia and bipolar disorder. *Schizophr Res.* **125**, 194–200
40. Rubenstein, J. L. R., and Merzenich, M. M. (2003) Model of autism: increased ratio of excitation/inhibition in key neural systems. *Genes Brain Behav.* **2**, 255–267
41. Sohal, V. S., and Rubenstein, J. L. R. (2019) Excitation-inhibition balance as a framework for investigating mechanisms in neuropsychiatric disorders. *Mol. Psych.* **24**, 1248–1257
42. Pace, C. N., Vajdos, F., Fee, L., Grimsley, G., and Gray, T. (1995) How to measure and predict the molar absorption coefficient of a protein. *Protein Sci.* **4**, 2411–2423
43. Laue, T. M., Shah, B. D., Ridgeway, T. M., and Pelletier, S. L. (1992). In: Harding, S., Rowe, A., eds. *Analytical Ultracentrifugation in Biochemistry and Polymer Science*, Royal Society of Chemistry, Cambridge, UK, 90–125
44. Schuck, P. (2000) Size-distribution analysis of macromolecules by sedimentation velocity ultracentrifugation and lamm equation modeling. *Biophys. J.* **78**, 1606–1619
45. Brautigam, C. A. (2015) Calculations and publication-quality illustrations for analytical ultracentrifugation data. *Met. Enzymol.* **562**, 109–133
46. Edgar, R. C. (2004) Muscle: multiple sequence alignment with high accuracy and high throughput. *Nucl. Acids Res.* **32**, 1792–1797
47. Krissinel, E., and Henrick, K. (2007) Inference of macromolecular assemblies from crystalline state. *J. Mol. Biol.* **372**, 774–797
48. Emsley, P., Lohkamp, B., Scott, W. G., and Cowtan, K. (2010) Features and development of Coot. *Acta Crystallogr. D Biol. Crystallogr.* **66**, 486–501
49. Rames, M., Yu, Y., and Ren, G. (2014) Optimized negative staining: a high-throughput protocol for examining small and asymmetric protein structure by electron microscopy. *J. Vis. Exp.* **15**, e51087
50. Zhang, L., Song, J., Newhouse, Y., Zhang, S., Weisgraber, K. H., and Ren, G. (2010) An optimized negative-staining protocol of electron microscopy for apoE4• POPC lipoprotein. *J. Lipid Res.* **51**, 1228–1236
51. Ludtke, S. J., Baldwin, P. R., and Chiu, W. (1999) EMAN: semiautomated software for high-resolution single-particle reconstructions. *J. Struct. Biol.* **128**, 82–97
52. Liu, J., Li, H., Zhang, L., Rames, M., Zhang, M., Yu, Y., *et al.* (2016) Fully mechanically controlled automated electron microscopic tomography. *Sci. Rep.* **6**, 29231
53. Kremer, J. R., Mastronarde, D. N., and McIntosh, J. R. (1996) Computer visualization of three-dimensional image data using IMOD. *J. Struct. Biol.* **116**, 71–76
54. Fernandez, J. J., Li, S., and Crowther, R. A. (2006) CTF determination and correction in electron cryotomography. *Ultramicroscopy* **106**, 587–596
55. Wu, H., Zhai, X., Lei, D., Liu, J., Yu, Y., Bie, R., *et al.* (2018) An algorithm for enhancing the image contrast of electron tomography. *Sci. Rep.* **8**, 16711
56. Zhai, X., Lei, D., Zhang, M., Liu, J., Wu, H., Yu, Y., *et al.* (2020) LoTToR: an algorithm for missing-wedge correction of the low-tilt tomographic 3D reconstruction of a single-molecule structure. *Sci. Rep.* **10**, 10489
57. Pettersen, E. F., Goddard, T. D., Huang, C. C., Couch, G. S., Greenblatt, D. M., Meng, E. C., *et al.* (2004) UCSF Chimera—a visualization system for exploratory research and analysis. *J. Comput. Chem.* **25**, 1605–1612
58. Takahashi, H., Katayama, K., Sohya, K., Miyamoto, H., Prasad, T., Matsumoto, Y., *et al.* (2012) Selective control of inhibitory synapse development by Slitrk3-PTPdelta trans-synaptic interaction. *Nat. Neurosci.* **15**, S1–S2
59. Takahashi, H., Arstikaitis, P., Prasad, T., Bartlett, T. E., Wang, Y. T., Murphy, T. H., *et al.* (2011) Postsynaptic TrkC and presynaptic PTPsigma function as a bidirectional excitatory synaptic organizing complex. *Neuron* **69**, 287–303

EDITORS' PICK: MDGA1 biological function is under 3D conformational control

60. Tanabe, Y., Naito, Y., Vasuta, C., Lee, A. K., Soumounou, Y., Linhoff, M. W., *et al.* (2017) IgSF21 promotes differentiation of inhibitory synapses via binding to neurexin2 α . *Nat. Commun.* **8**, 408
61. Lu, S., Cao, Y., Fan, S.-B., Chen, Z.-L., Fang, R.-Q., He, S.-M., *et al.* (2018) Mapping disulfide bonds from sub-micrograms of purified proteins or micrograms of complex protein mixtures. *Biophys. Rep.* **4**, 68–81
62. Coghlan, J., Benet, A., Kumaran, P., Ford, M., Veale, L., Skilton, S. J., *et al.* (2022) Streamlining the characterization of disulfide bond shuffling and protein degradation in IgG1 biopharmaceuticals under native and stressed conditions. *Front. Bioeng. Biotechnol.* **10**, 862456
63. Bailey, A. O., Huguet, R., Mullen, C., Syka, J. E. P., and Russell, W. K. (2022) Ion-ion charge reduction addresses multiple challenges common to denaturing intact mass analysis. *Anal. Chem.* **94**, 3930–3938
64. UniProt, C. (2022) UniProt: the universal protein knowledgebase in 2023. *Nucl. Acids Res.* **51**, D523–D531



Hubert Lee is a Ph.D. candidate in the Structural Biology and Biophysics Program at the University of Texas Medical Branch. He studies the molecular mechanisms of synaptic organizing molecules. Hubert is using protein engineering to interrogate the impact of different conformations of the synaptic organizer, MDGA1, on its ability to regulate neurexin–neuroligin trans-synaptic bridges. Overall, the work contributes to a better understanding of the complex protein interaction networks at synapses and the important roles of structure and spatial effects on function.



Nicolas Chofflet is a Ph.D. candidate in the Integrated Program in Neuroscience at McGill University. He is interested in deciphering how cell adhesion molecules mediate neural circuits assembly and maturation in the brain. MDGA molecules are key regulators of GABAergic synapse development, but their structure-to-function relationships are not well understood. Nicolas is leveraging engineered MDGA1 molecules to probe the ability of MDGA1 to tune inhibitory synapses assembly through regulation of neurexin–neuroligin protein complexes.



Jianfang Liu, Ph.D., is a project scientist at Lawrence Berkeley National Laboratory (LBNL). His research focuses primarily on developing the cryo-electron tomography technique, individual particle electron tomography (IPET), to determine the 3D structure of a single molecule without averaging. This technique allows for the identification of macromolecule structural variations and generates snapshots of dynamic and flexible macromolecules. IPET is very well suited to study large, flexible multidomain synaptic organizers, like MDGA1, which are otherwise very difficult to study.

Designer molecules of the synaptic organizer MDGA1 reveal 3D conformational control of biological function

Hubert Lee^{1,2,*}, Nicolas Chofflet^{3,4,*}, Jianfang Liu^{5,*}, Shanghua Fan^{1,2}, Zhuoyang Lu⁵, Martin Resua Rojas³, Patrick Penndorf³, Aaron O. Bailey⁶, William K. Russell⁶, Mischa Machius^{1,2}, Gang Ren^{5,#}, Hideto Takahashi^{3,4,7,8,#}, Gabby Rudenko^{1,2,#}

SUPPLEMENTAL INFORMATION

- **Tables S1-S2**
- **Figures S1-S6**

SUPPORTING INFORMATION

Methods

NanoLC-MS/MS disulfide mapping analysis: Samples of purified MDGA1 WT and mutants were prepared for nanoLC-MS/MS disulfide mapping analysis by changing the buffer to 100 mM Tris, pH 6.5 using a P-6 size exclusion spin column (BioRad). Samples were then treated with n-ethylmaleimide (NEM) to alkylate free thiols (2 mM final concentration, incubating for 2 h at 37°C) and subsequently subjected to proteolysis using trypsin at an enzyme:substrate ratio of 1:20 for 8 h at 37°C (61). Trypsin activity was quenched by adding formic acid to a final concentration of 1% (v/v). Prepared samples were analyzed by nanoLC-MS/MS (nanoRSLC, ThermoFisher) using an Aurora series (Ion Opticks) reversed-phase HPLC column (25 cm length x 75 µm inner diameter) eluting into an Orbitrap Eclipse mass spectrometer. Peptides were separated using a 120 min method (mobile phase A = 0.1% (v/v) formic acid (Thermo Fisher), mobile phase B = 99.9% (v/v) acetonitrile with 0.1% (v/v) formic acid (Thermo Fisher); hold 1% (v/v) B for 5 min, 1-6% (v/v) B over 1 min, 6-25% (v/v) B over 100 min, and 25-50% (v/v) B over 15 min) at a flow rate of 300 µL/min. Eluted peptide ions were analyzed using a data-dependent acquisition (DDA) method with resolution settings of 120,000 and 15,000 (at m/z 200) for MS1 and MS2 scans, respectively. DDA-selected peptides were fragmented using electron transfer dissociation using instrument-controlled charge state-calibrated reaction times. Raw MS data were searched using the disulfide mapping workflow in Byos (v4.5-53) using trypsin as the selected protease (62). Disulfide pair abundances were calculated using the extracted ion chromatogram (XIC) peak areas summed for each charge state detected. Cysteine site occupancy was calculated per each cysteine site as a fractional abundance using the XIC peak area sum of all disulfide pairs and lone cysteine forms (including free thiols and NEM-alkylated cysteines).

Denaturing LC-MS Intact Mass Analysis. Purified MDGA WT was analyzed by LC-MS directly to measure the profile of glycosylated isoforms of the intact protein. MDGA protein sample (0.1 mg/ml) was injected as a volume of 1 µL into a flow path (200 µL/min) of denaturing mobile phase (30% (v/v) acetonitrile, 0.1% (v/v) formic acid, 0.2% (v/v) trifluoroacetic acid) and desalted using size exclusion (BEH SEC200, 4 x 30 mm, 1.7 µm particle size; Waters) performed using a Vanquish Horizon UHPLC system (Thermo Fisher). Desalted proteins were eluted directly into an Orbitrap Eclipse mass spectrometer equipped with an H-ESI ion source and proton transfer charge reduction (PTCR) such that denatured intact protein isoforms were ionized by electrospray, PTCR-reacted, and then detected using a resolution of 15,000 (at 200 m/z) (63). Raw MS data were analyzed by charge state deconvolution using Byos v4.5-53 Intact workflow.

		MDGA1 WT		MDGA1 T ¹³⁵ C/N ³¹³ C	MDGA1 V ³¹⁴ D	MDGA1 T ³³³ C/Y ⁵¹⁹ C	MDGA1 I ³³⁶ D	MDGA1:NLGN2(+A)
Conditions		LS	HS	HS	HS	HS	HS	LS
Class Averaging	Micrographs	8	49	47	36	48	46	23
	Particles	1,114	10,661	4,511	3,780	9,047	3,352	1,828
	Classes	25	236	102	84	200	74	n.d.
Molecular Shape Analysis	Micrographs	n.d.	5	5	5	5	5	n.d.
	Particles	n.d.	800	421	473	896	399	n.d.

Table S1. Negative-staining electron microscopic (NS-EM) images for Class Averaging and Molecular Shape Analysis. Reference-free class averages were calculated from particles picked from micrographs. For molecular shape statistics, all reasonable particles were picked from five typical micrographs to avoid sampling bias. HS, high-salt (high ionic strength) conditions (10 mM HEPES, 500 mM NaCl, pH 8); LS, low-salt (low ionic strength) conditions (10 mM HEPES, 50 mM NaCl, pH 8); n.d., not done or not determined.

UniProt ID	Species	UniProt ID	Species
A0A3Q0G637	Alligator sinensis	I3ME41	Ictidomys tridecemlineatus
A0A8B9I24	Amazona collaria	A0A287CTS9	Ictidomys tridecemlineatus
A0A493TVQ2	Anas platyrhynchos platyrhynchos	A0A8C5KFI4	Jaculus jaculus
U3IEI6	Anas platyrhynchos platyrhynchos	A0A8C5J9P6	Junco hyemalis
A0A8B9U5M9	Anas zonorhyncha	A0A6J0GKI3	Lepidothrix coronata
A0A803T477	Anolis carolinensis	A0A340Y4P1	Lipotes vexillifer
A0A803TBQ9	Anolis carolinensis	A0A667GLJ9	Lynx canadensis
A0A803TJA0	Anolis carolinensis	A0A2K5VYN8	Macaca fascicularis
G1KIU8	Anolis carolinensis	A0A2K5VYH6	Macaca fascicularis
R4GAC6	Anolis carolinensis	F6S264	Macaca mulatta
A0A8B9CQ01	Anser brachyrhynchus	I2CVH3	Macaca mulatta
A0A8B9CRV7	Anser brachyrhynchus	A0A2K6D279	Macaca nemestrina
A0A8B9CSD5	Anser brachyrhynchus	A0A2K6D283	Macaca nemestrina
A0A8B9CU45	Anser brachyrhynchus	A0A8C5X632	Malurus cyaneus samueli
A0A8B9E1X0	Anser cygnoid	A0A2K5YSP4	Mandrillus leucophaeus
A0A2K5EZK0	Aotus nancymaae	A0A2K5YSP1	Mandrillus leucophaeus
A0A2K5EZF8	Aotus nancymaae	A0A2K5YSP2	Mandrillus leucophaeus
A0A2K5EZI5	Aotus nancymaae	A0A8C6AEL4	Marmota marmota marmota
A0A8B7INP3	Apteryx mantelli mantelli	A0A8C6AG51	Marmota marmota marmota
A0A8B9PXH7	Apteryx owenii	A0A834QYT1	Marmota monax
A0A663EV12	Aquila chrysaetos chrysaetos	A0A8C6JDY3	Melopsittacus undulatus
A0A663LL67	Athene cucularia	A0A1U7RDM5	Mesocricetus auratus
A0A384BE34	Balaenoptera acutorostrata scammoni	A0A8C5UNR6	Microcebus murinus
A0A8C0D2W1	Balaenoptera musculus	A0A8J6L3D1	Microtus ochrogaster
A0A4W2FGA0	Bos indicus x Bos taurus	A0A8C6BNI7	Monodon monoceros
A0A4W2C089	Bos indicus x Bos taurus	Q0PMG2	Mus musculus
A0A4W2DV33	Bos indicus x Bos taurus	D3Z499	Mus musculus
A0A4W2HH40	Bos indicus x Bos taurus	A0A8C6GVQ3	Mus spicilegus
L8HZ53	Bos mutus	A0A8C6GWY4	Mus spicilegus
A0A8B9WX52	Bos mutus grunniens	A0A7J7WWT7	Myotis myotis
F1MHX8	Bos taurus	A0A8C6Y8D5	Naja naja
A0A8C0F0K4	Bubo bubo	A0A8C6Y968	Naja naja
A0A8C0B3F6	Buteo japonicus	A0A8C6QR19	Nannospalax galili
A0A8C3JBF2	Calidris pygmaea	A0A8C6QRW9	Nannospalax galili
A0A8I3W577	Callithrix jacchus	A0A2Y9GR16	Neomonachus schauinslandi
A0A8I3WN48	Callithrix jacchus	A0A341D7K0	Neophocaena asiaeorientalis
F6YRU2	Callithrix jacchus	A0A8C7BDJ7	Neovison vison
U3FS14	Callithrix jacchus	A0A2U3WLP9	Odobenus rosmarus divergens
A0A3Q7NDI3	Callorhinus ursinus	F7BLY1	Ornithorhynchus anatinus
A0A8C0K4H2	Canis lupus dingo	A0A8B6ZR73	Orycteropus afer afer
A0A8C0QX76	Canis lupus dingo	A0A8C8EDI2	Otus sunia
A0A8C0QX78	Canis lupus dingo	A0A6P7D6I2	Ovis aries
A0A8C0QX80	Canis lupus dingo	K7BUY7	Pan troglodytes
A0A8C0MPX8	Canis lupus familiaris	A0A2I3T204	Pan troglodytes
A0A8C0MVL5	Canis lupus familiaris	K7B6F4	Pan troglodytes
A0A8C0T7W1	Canis lupus familiaris	A0A8C8WBR8	Panthera leo
A0A8C0TDG7	Canis lupus familiaris	A0A096NHW1	Papio anubis
A0A8I3NF61	Canis lupus familiaris	A0A096NHW2	Papio anubis
A0A8I3NKI0	Canis lupus familiaris	A0A8I5R7N8	Papio anubis
A0A452EYK6	Capra hircus	A0A8I5R9H3	Papio anubis
A0A452EYK1	Capra hircus	A0A8C8TDS2	Peromyscus maniculatus bairdii
A0A452EYL0	Capra hircus	A0A6P5LAA3	Phascolarctos cinereus
A0A452EYM1	Capra hircus	A0A669P3D1	Phasianus colchicus
A0A452EYN1	Capra hircus	A0A669PIP5	Phasianus colchicus
A0A8C0WTG8	Castor canadensis	A0A834AP21	Phyllostomus discolor

A0A8C0WWP4	Castor canadensis	A0A8C9IIH5	Ptilocolobus tephrosceles
A0A8C3YFA1	Catagonus wagneri	A0A8C9IMC1	Ptilocolobus tephrosceles
A0A8C3TUT3	Catharus ustulatus	A0A7J7YMG2	Pipistrellus kuhlii
A0A8C3TW51	Catharus ustulatus	A0A7J7YNI1	Pipistrellus kuhlii
A0A286Y479	Cavia porcellus	A0A6J2HU52	Pipra filicauda
H0UUF5	Cavia porcellus	A0A670I5G0	Podarcis muralis
A0A2K5PHQ2	Cebus imitator	H2PIX1	Pongo abelii
A0A2K5PHP5	Cebus imitator	A0A8I5UXB6	Pongo abelii
A0A2K5P7B9	Cercocebus atys	A0A8C8ZCE9	Prolemur simus
A0A2K5P7B8	Cercocebus atys	A0A2K6EIN1	Propithecus coquereli
A0A8C0JAZ5	Chelonoidis abingdonii	A0A2K6EIN3	Propithecus coquereli
A0A8C2VK71	Chinchilla lanigera	A0A670YG06	Pseudonaja textilis
A0A8C2VQD5	Chinchilla lanigera	A0A6P3Q248	Pteropus vampyrus
A0A0D9RDP6	Chlorocebus sabaeus	P85171	Rattus norvegicus
A0A8C3INS8	Chrysemys picta bellii	A0A140TAF4	Rattus norvegicus
A0A6I9JG75	Chrysochloris asiatica	A0A8I6AGZ5	Rattus norvegicus
A0A8C3L6V6	Chrysolophus pictus	A0A671DNE8	Rhinolophus ferrumequinum
A0A2K5IE01	Colobus angolensis palliatus	A0A7J7YSF7	Rhinolophus ferrumequinum
A0A2K5IEA6	Colobus angolensis palliatus	A0A2K6P215	Rhinopithecus roxellana
A0A8C3DXG9	Corvus moneduloides	A0A2K6P209	Rhinopithecus roxellana
A0A8C2TDG2	Coturnix japonica	A0A7J8KCB5	Rousettus aegyptiacus
A0A8C2MQA7	Cricetulus griseus	A0A7J8KCH9	Rousettus aegyptiacus
A0A8C2MSA2	Cricetulus griseus	A0A2K6SDT8	Saimiri boliviensis boliviensis
A0A7M4ET58	Crocodylus porosus	A0A2K6SDT6	Saimiri boliviensis boliviensis
A0A7M4ETL0	Crocodylus porosus	A0A2K6SDU7	Saimiri boliviensis boliviensis
A0A8C0U1H1	Cyanistes caeruleus	A0A8D0BEJ8	Salvator merianae
A0A8C0U3M4	Cyanistes caeruleus	G3WWI1	Sarcophilus harrisi
A0A8C3R6A3	Cyanoderma ruficeps	G3WWI0	Sarcophilus harrisi
A0A2Y9NTZ3	Delphinapterus leucas	A0A8D2AY20	Sciurus vulgaris
A0A1S3G9U7	Dipodomys ordii	A0A8C9NFG6	Serinus canaria
A0A8C4JMX2	Dromaius novaehollandiae	A0A8D0G5L0	Sphenodon punctatus
A0A2Y9JEP5	Enhydra lutris kenyonii	A0A672URH8	Strigops habroptila
F6YDA3	Equus caballus	A0A672USS1	Strigops habroptila
A0A3Q2L5J4	Equus caballus	A0A8D0F9J6	Strix occidentalis caurina
A0A1S2ZDV2	Erinaceus europaeus	A0A673SVW3	Suricata suricatta
A0A8C4TXX7	Falco tinnunculus	A0A673SVY3	Suricata suricatta
M3W6F6	Felis catus	A0A4X1SRT3	Sus scrofa
U3K9L0	Ficedula albicollis	F1RVR8	Sus scrofa
A0A8J6A5K3	Galemys pyrenaicus	A0A8D2GE59	Theropithecus gelada
Q0WYX8	Gallus gallus	A0A8D2GEG1	Theropithecus gelada
A0A3Q2TWX8	Gallus gallus	A0A8D2GI33	Theropithecus gelada
A0A3Q3A2A3	Gallus gallus	A0A2Y9DR82	Trichechus manatus latirostris
A0A8N5ETA6	Geospiza fortis	A0A452Q8M6	Ursus americanus
A0A8C3MSU6	Geospiza parvula	A0A452Q9F8	Ursus americanus
A0A452H954	Gopherus agassizii	A0A3Q7TR82	Ursus arctos horribilis
A0A452H9S2	Gopherus agassizii	A0A8D2IZQ4	Varanus komodoensis
A0A8C4WAY7	Gopherus evgoodei	A0A6J0AER2	Vicugna pacos
G3RYJ7	Gorilla gorilla gorilla	A0A3Q7RLZ5	Vulpes vulpes
G3QME6	Gorilla gorilla gorilla	A0A8D2MUE0	Zonotrichia albicollis
Q8NFP4	Homo sapiens	A0A8D2MXJ3	Zonotrichia albicollis
A0A3B3IU48	Homo sapiens	A0A8D2MY10	Zonotrichia albicollis

Table S2. MDGA1 Multi-Sequence Alignment (MSA): Listed are the UniProt identifiers (64) and species names of all sequences used for the MSA.

Figures

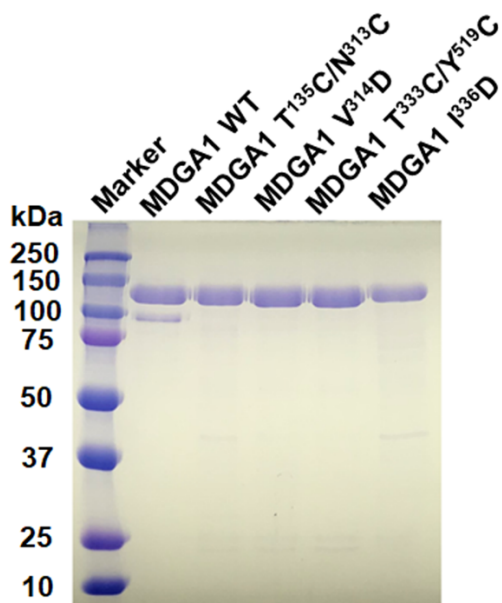
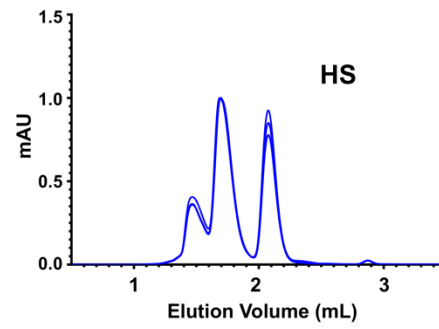
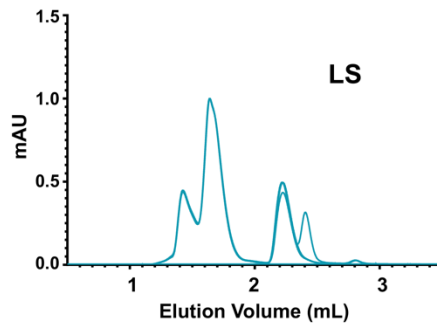
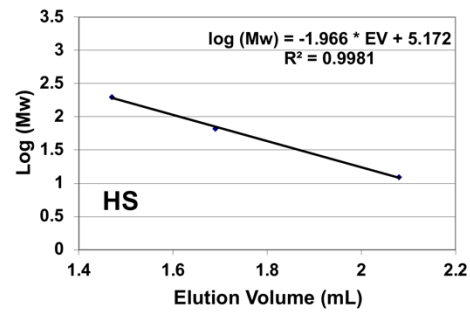
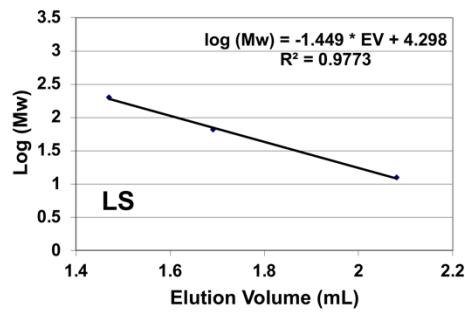


Figure S1. SDS-PAGE of over-expressed and purified proteins used in this study. MDGA1 WT and MDGA1 mutants (T¹³⁵C/N³¹³C, V³¹⁴D, T³³³C/Y⁵¹⁹C, I³³⁶D). To assess protein purity, samples (6 μ gr/lane) were analyzed using 12% SDS-PAGE stained with Coomassie blue.

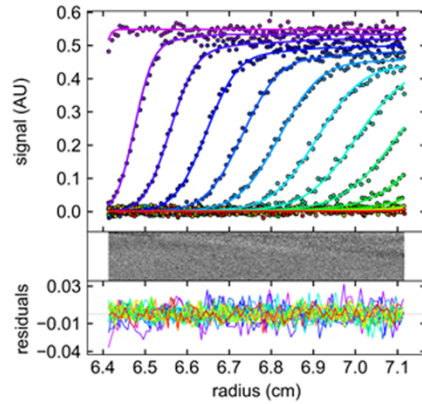
A)

Size Exclusion Chromatography - Calibration

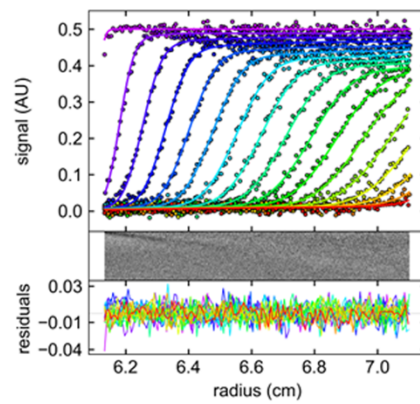
	Buffer	Calibration Standard	Mw [kDa]	Stokes radius, R_s [nm]	Avg. EV \pm SD [mL]
LS	10 mM HEPES, 50 mM NaCl, pH 8	β -amylase	200	5.4	1.42 \pm 0.01
		albumin	66	3.5	1.64 \pm 0.00
		cytochrome C	12.4	1.7	2.22 \pm 0.01
HS	10 mM HEPES, 500 mM NaCl, pH 8	β -amylase	200	5.4	1.47 \pm 0.00
		albumin	66	3.5	1.69 \pm 0.01
		cytochrome C	12.4	1.7	2.08 \pm 0.00

**B)**

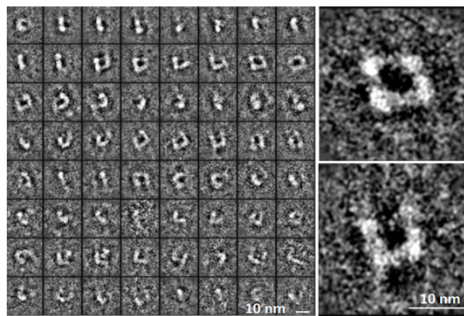
LS



HS

**C)**

LS



HS

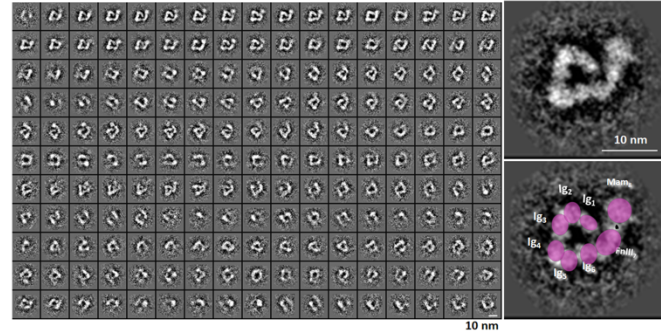


Figure S2. Characterization of MDGA1 WT. A) Size exclusion chromatography (SEC) elution profiles of calibration standards (β -amylase, albumin, cytochrome C) at low ionic strength (LS, 10 mM HEPES, 50 mM NaCl, pH 8) and high ionic strength (HS, 10 mM HEPES, 500 mM NaCl, pH 8) executed in triplicate. The elution volumes (EV) deviated by less than 0.02 ml between experiments. One replicate run for the LS conditions had a fourth extraneous (noise) peak. A table summarizes the calibration standards used, their molecular weights, hydrodynamic radii (R_s), and the mean EVs plus standard deviation (SD) from the triplicate runs, under both LS and HS conditions. SEC calibration plots (EV vs. $\log(Mw)$) under LS (left) and HS (right) conditions are shown as well. **B)** Representative sedimentation velocity profiles and residual plots under LS (left) and HS (right) conditions. **C)** Negative-staining electron microscopy (NS-EM) of MDGA1 WT under LS conditions (left). Class averages were obtained from 1,114 particles. Zoomed-in images of two representative class averages with the best contrast are shown. NS-EM of MDGA1 WT under HS conditions (right). Class averages were obtained from 10,661 particles. Zoomed-in images of one representative class average for the compact form revealing good contrast are also shown. Purple oval discs indicate the location of individual MDGA1 domains (bottom right).

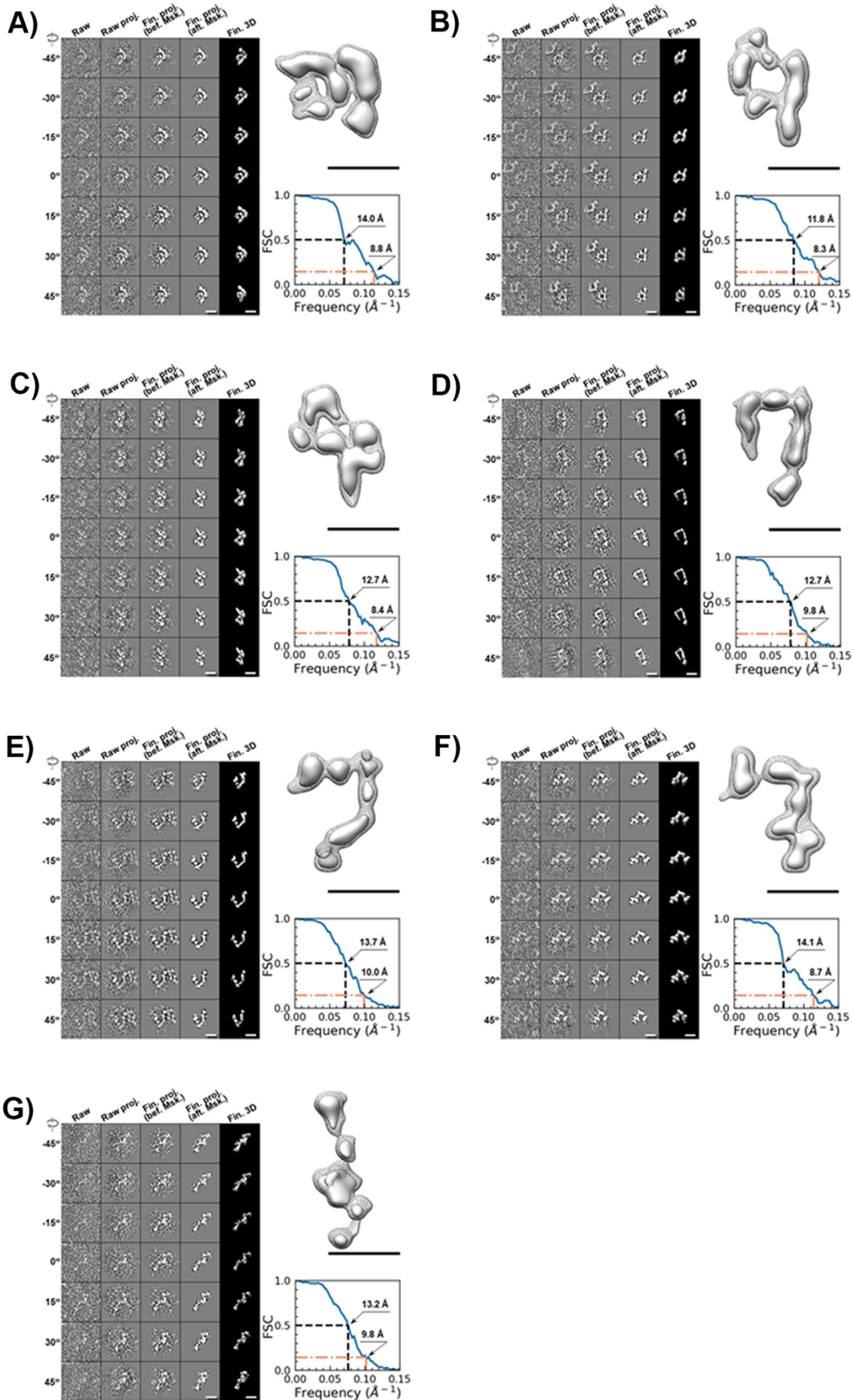


Figure S3. Individual particle electron tomography (IPET) 3D reconstruction of seven MDGA1 WT particles (A-G) taken from the image shown in Fig. 2F. IPET 3D reconstruction process for each targeted particle with seven representative tilt images gradually aligned via an iterative refinement for 3D reconstruction, the final 3D density map of the targeted particle, and the resolution estimated by Fourier Shell Correlation (FSC) analysis between two half reconstructions from odd and even numbers of tilt images. Scale bars represent 10 nm.

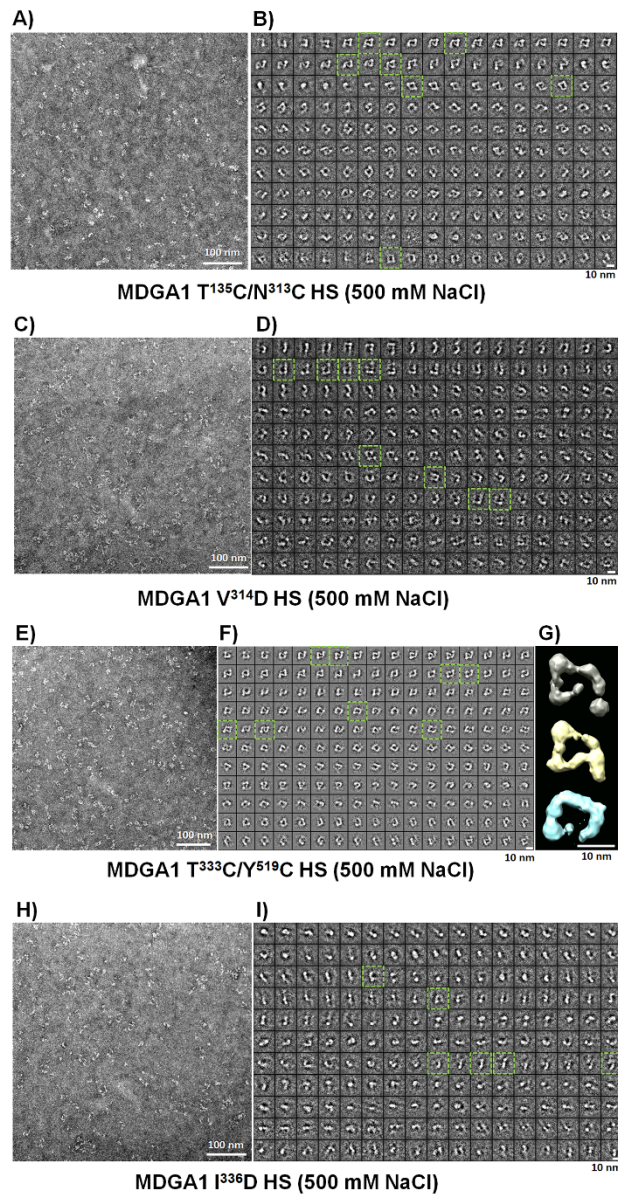


Figure S4. NS-EM images and class averages of MDGA1 designer mutants under high ionic strength conditions (HS; 10 mM HEPES, 500 mM NaCl, pH 8). **A)** Survey micrographs of MDGA1 T¹³⁵C/N³¹³C particles. **B)** Reference-free class averages achieved from 4,511 MDGA1 T¹³⁵C/N³¹³C particles, 187 out of 289 are shown here. **C)** Survey micrographs of MDGA1 V³¹⁴D particles. **D)** Reference-free class averages achieved from 3,780 particles MDGA1 V³¹⁴D particles, 187 out of 255 are shown here. **E)** Survey micrographs of MDGA1 T³³³C/Y⁵¹⁹C particles. **F)** Reference-free class averages achieved from 9,047 MDGA1 T³³³C/Y⁵¹⁹C particles, 187 out of 619 are shown here. **G)** Isosurface of three representative density maps of MDGA1 T³³³C/Y⁵¹⁹C particles that were reconstructed using a conventional single-particle averaging method. **H)** Survey micrographs of MDGA1 I³³⁶D particles. **I)** Reference-free class averages achieved from 3,352 MDGA1 I³³⁶D particles, 187 out of 310 are shown here. Representative class averages shown also in [Fig. 4E-H](#) are boxed here with a green dotted line.

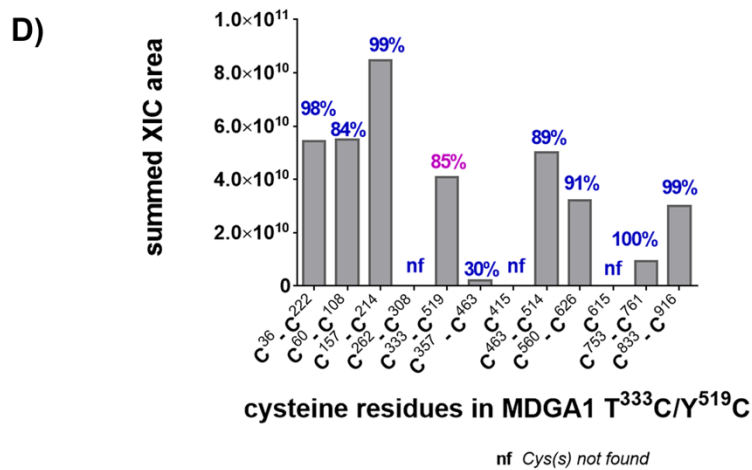
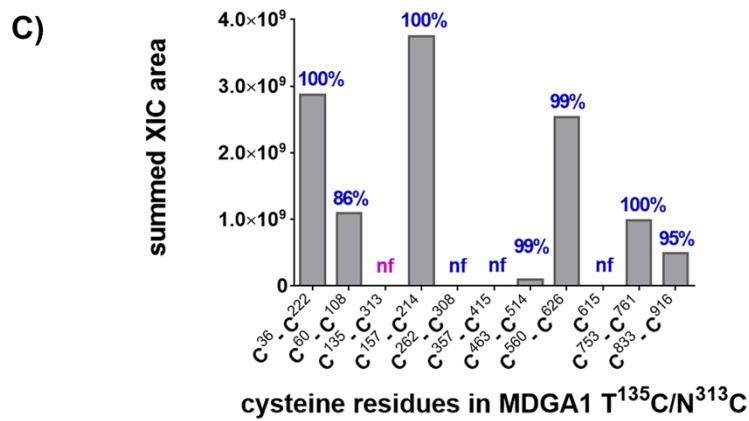
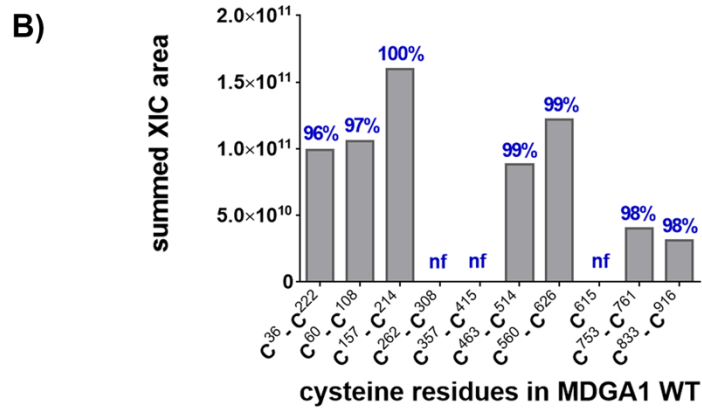
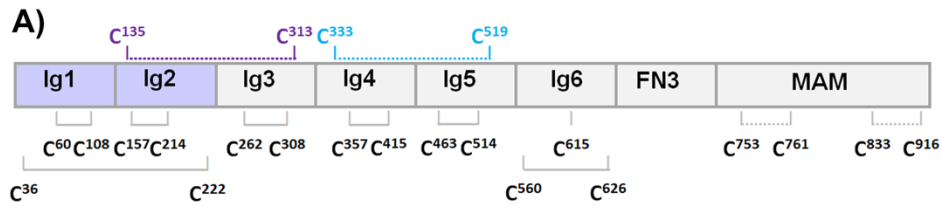
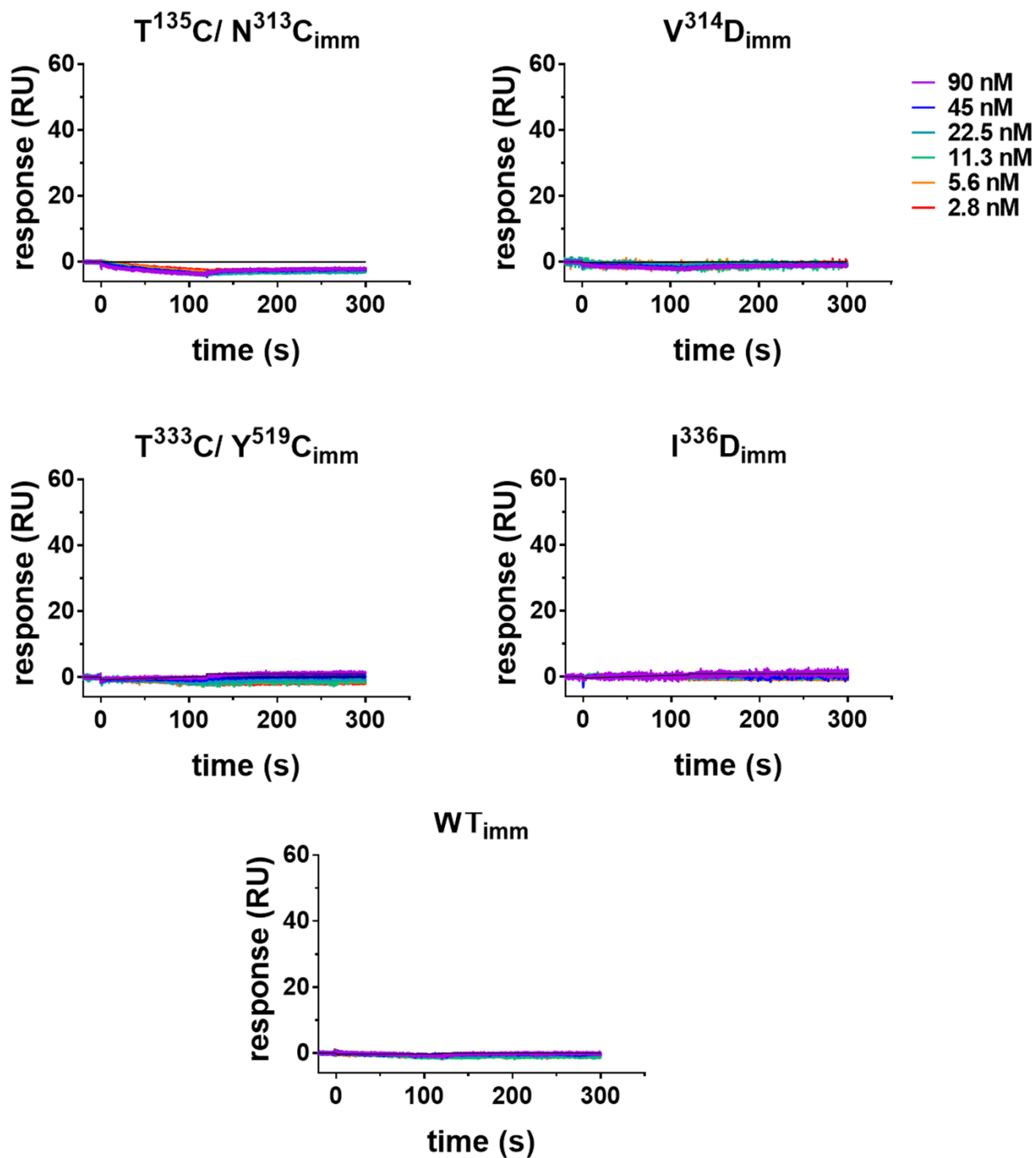


Figure S5. Mass Spectrometry validation of MDGA1 T¹³⁵C/N³¹³C and MDGA1 T³³³C/Y⁵¹⁹C. **A)** Schematic of the MDGA1 domain structure with native cysteine residues (black, bottom) and engineered cysteines (purple or cyan, top) indicated. Putative disulfide bonds are indicated as connecting horizontal lines between cysteine pairs. **B-D)** For each MDGA1 sample, bar graphs show the identification of protein fragments that contained cysteines (found as free cysteines or paired as disulfide bonds) expressed as the summed extracted ion chromatogram peak (XIC) area. The abundance of the most prevalent fragment carrying the first cysteine of each pair (or just the free cysteine) is indicated above each bar as a percentage (%) of all fragments identified carrying that particular cysteine. Percentages in blue indicate native cysteines and in magenta engineered cysteines. 'nf' indicates no protein fragment carrying that particular cysteine or cysteine pair was found.



Immobilized Ligand	Analyte	$K_D \pm SD$ (nM)	Response (RU)	Immobilized (RU)	N
MDGA1 WT	NLGN2 (+A) Mut 1	n.d.	[0 – 8]	[403 – 408]	5
MDGA1 $T^{135}C/N^{313}C$	NLGN2 (+A) Mut 1	n.d.	[0 – 8]	[413 – 425]	3
MDGA1 $V^{314}D$	NLGN2 (+A) Mut 1	n.d.	[0 – 10]	[462 – 610]	4
MDGA1 $T^{333}C/Y^{519}C$	NLGN2 (+A) Mut 1	n.d.	[0 – 7]	[485]	2
MDGA1 $I^{336}D$	NLGN2 (+A) Mut 1	n.d.	[1 – 6]	[483]	2

Figure S6. Surface plasmon resonance (SPR) of MDGA1 constructs shows that they do not interact with NLGN2(+A) Mut1. Binding of soluble NLGN2(+A) Mut 1 to MDGA1-coupled sensors using a concentration range of 0-90 nM (top right). Representative sensorgrams (colored curves) are fitted to a 1:1 bimolecular interaction model (black curves; see Materials & Methods). 'Response' (in RU) refers to the amount of soluble NLGN2(+A) Mut1 bound (Analyte). 'Immobilized' (in RU) refers to the amount of the different MDGA1 forms immobilized to the C1 sensor chip (Ligand). NLGN2(+A) Mut1 concentrations are expressed as a function of the Mw of the NLGN2 dimer because the MDGA1 forms are sparsely immobilized on the SPR chip and thus bind soluble NLGN2 dimers to form an MDGA1:NLGN2(+A)_{dimer} complex. Note: a different representative sensorgram for MDGA1 WT binding to NLGN2(+A) Mut 1 is shown in [Fig. 7](#). n.d., K_D values not determined.